Automated Earthquake Detection and Local Travel Time Tomography in the South-Central Andes (32–35°S)

Jean-baptiste Ammirati, Antonio Villaseñor, Sébastien Chevrot, Gabriel Easton, Maximilien Lehujeur, Sergio Ruiz, María Constanza Flores

JGR Solid Earth

RESEARCH ARTICLE
10.1029/2022JB024097

Automated Earthquake Detection and Local Travel Time Tomography in the South-Central Andes (32–35°S): Implications for Regional Tectonics

Jean-Baptiste Ammirati[1,2], Antonio Villaseñor[3], Sébastien Chevrot[2], Gabriel Easton[1], Maximilien Lehujeur[4], Sergio Ruiz[5], and María Constanza Flores[6]

[1]Departamento de Geología, Universidad de Chile, Santiago, Chile, [2]Géosciences Environnement Toulouse, Observatoire Midi-Pyrénées, Université Paul Sabatier, CNRS, IRD, Toulouse, France, [3]Institute of Marine Sciences, ICM-CSIC, Barcelona, Spain, [4]Université Gustave Eiffel, Paris, France, [5]Departamento de Geofísica, Universidad de Chile, Santiago, Chile, [6]Centro Sismológico Nacional, Santiago, Chile

Key Points:

- A large number of earthquakes detected using a deep-learning approach are used for local earthquake tomography
- The obtained 3-D seismic wave velocity structure is used to relocate the seismicity catalog
- Earthquake locations suggest a west-dipping major structure that we interpret to have contributed to the uplift of the South-Central Andes

Supporting Information:

Supporting Information may be found in the online version of this article.

Correspondence to:

J.-B. Ammirati,
jbaptiste@ing.uchile.cl

Citation:

Ammirati, J.-B., Villaseñor, A., Chevrot, S., Easton, G., Lehujeur, M., Ruiz, S., & Flores, M. C. (2022). Automated earthquake detection and local travel time tomography in the South-Central Andes (32–35°S): Implications for regional tectonics. *Journal of Geophysical Research: Solid Earth*, *127*, e2022JB024097. https://doi.org/10.1029/2022JB024097

Received 24 JAN 2022
Accepted 31 MAR 2022

Author Contributions:

Conceptualization: Jean-Baptiste Ammirati
Data curation: María Constanza Flores
Formal analysis: Jean-Baptiste Ammirati, Antonio Villaseñor, Sébastien Chevrot, Gabriel Easton, Sergio Ruiz
Funding acquisition: Jean-Baptiste Ammirati
Methodology: Jean-Baptiste Ammirati, Antonio Villaseñor, Sébastien Chevrot, Sergio Ruiz
Resources: Jean-Baptiste Ammirati, Sébastien Chevrot, María Constanza Flores
Software: Jean-Baptiste Ammirati, Antonio Villaseñor, Maximilien Lehujeur
Visualization: Jean-Baptiste Ammirati

Abstract In the South-Central Andes, the crustal structures driving the tectonic evolution of the Andean Cordillera remain unresolved. So far, most seismological studies focused on the subduction interface, leaving crustal seismicity and its relationship with crustal deformation and Andean volcanism mostly unconstrained. However, because of their large number compared to higher magnitude events, the characterization of small-magnitude crustal earthquakes is key to identify active structures and better constrain the tectonic models. In this work, we exploit 53 months of continuously recorded, three-component waveforms from the permanent seismic network in central Chile using a deep-learning approach to improve the detection of small-magnitude earthquakes. To increase station coverage, we also use the seismic phases obtained from a previous temporary seismic deployment. We use the obtained seismicity catalog to refine tomographic models of that region, revealing a more detailed architecture of the Chilean forearc. Travel times calculated in the new 3-D velocity model allowed us to locate ∼14,000 earthquakes. Refined double-difference relocations of ∼4,900 events located beneath the West Andean Thrust suggest a large-scale, west-dipping structure which, together with the west-verging tectonic front, likely contributed to the uplift and crustal deformation during the past ∼20 Myr.

Plain Language Summary The occurrence of earthquakes is closely related to plate tectonics and in particular, the creation of mountain ranges and their evolution over very long periods of time. In order to better understand how these processes work in the Andes of Central Chile, we analyze more than 4 years of earthquake records using a machine learning algorithm. This technique allows us to automatically and reliably detect very small earthquakes, that are, in general, missing in the seismicity catalogs. Since they are also more numerous, we can use them to improve the geophysical images and reveal more details of crustal structures. We find that most of the superficial earthquakes beneath the Andean Cordillera are aligned with a major structure, dipping toward the west. This structure accommodates processes of shortening and uplifting directly related to the construction of the Andes.

1. Introduction

Stretching over more than 4,000 km along the western margin of South America, the Central Andes are produced by the subduction of the Nazca plate under the South American Plate, resulting in one of the most remarkable orogens on Earth (Figure 1). The subduction of the Nazca plate is linked to the occurrence of numerous large-magnitude megathrust earthquakes, such as the 2010 (Mw 8.8) Maule; 2014 (Mw 8.2) Iquique; 2015 (Mw 8.3) Illapel; and 2016 (Mw 7.6) Chiloe earthquakes, to name a few major events that recently occurred along the Chilean margin (Delouis et al., 2010; Lay et al., 2014; Ruiz et al., 2016, 2017; Ruiz & Madariaga, 2018).

Our study region lies in the South-Central Andes segment, between 32°S and 35°S (Figure 1). At these latitudes, the Andean belt is about 150 km wide and displays an average elevation of ∼3,000 m, with several peaks close to 6,000 m, culminating with the Aconcagua, the tallest peak of the Americas (6,961 m a.s.l.; −32.6°S; −70.0°W). Over the years, the gradual densification of seismological instrumentation in Chile allowed to identify a sustained crustal seismic activity related to deformation processes in the South-Central Andes. Barrientos et al. (2004) used an improved regional 1D velocity model to relocate ∼20 years of seismicity recorded by the Chilean seismological center (CSN) resulting in a more clustered hypocenter distribution beneath the South-Central Andes.

Writing – original draft: Jean-Baptiste Ammirati, Antonio Villaseñor
Writing – review & editing: Jean-Baptiste Ammirati, Antonio Villaseñor, Sébastien Chevrot, Gabriel Easton, Sergio Ruiz

However, due to poor seismological station coverage at that time, their location uncertainties were still too large for accurate tectonic interpretations. Farías et al. (2010) inverted P- and S-wave travel times also corresponding to events from the CSN catalog as well as a small (seven seismometers) temporary array. Their resulting 3D model was quite smooth and did not allow them to identify crustal structure but helped to relocate ∼7,200 earthquakes, mostly coming from the subduction interface. Their images allowed them to build one of the few tectonic models available for the study area that is constrained by both surface and seismological observations. In addition to the Chilean permanent network (Barrientos & National Seismological Center (CSN) Team, 2018), several seismic temporary experiments have been carried out in the study region. They resulted in large-scale tomographic images mostly focusing on the Nazca subduction dynamics (Porter et al., 2012), differences and similarities between flat versus "normal" subduction (Marot et al., 2014), intraplate seismicity and slab dehydration (Marot et al., 2013; Wagner et al., 2005).

It is important to note that none of these studies focused on improving the completeness of the crustal seismicity catalogs. It is only recently (2013–2017) that the densification of the Chilean seismic network in central Chile (Barrientos & National Seismological Center (CSN) Team, 2018) allowed the systematic detection and characterization of ∼1,000 small-magnitude (M ∼ 2) crustal earthquakes located beneath the South-Central Andes, over a period of ∼2 years (Ammirati et al., 2019). Although very promising, these results highlighted the need to switch from a traditional, time-consuming semi-automatic processing to a fully automated approach in order to process large amounts of continuous waveforms in a more time-efficient and rigorous manner.

The aim of this paper is to provide a more complete crustal seismicity catalog with improved hypocenter locations in order to identify the structures accommodating the deformation in the crust of the South-Central Andes. For this purpose, (a) we analyze 4.4 years of continuous broadband waveforms to automatically detect and pick the P and S phases produced by local seismicity. (b) We investigate seismic velocity variations in our study region by inverting the corresponding seismic phase travel times. (c) We use the resulting 3-D tomographic model to relocate the seismicity obtained in (a). (d) Finally, we improve our seismicity catalog with double-difference relocations and add moment tensor inversions. The results are used to reassess existing crustal deformation models and discuss the implications for mountain building processes and tectonic evolution of the South-Central Andes.

2. Geological Setting

The subduction along the western margin of South America began at the end of the early Cretaceous, during the breakup of Gondwana (Ramos, 2000). However, the Andean orogeny as currently observed, only began during the Eocene at the earliest. Ages of the subducting Nazca plate along the South-American margin, are relatively young (20–60 Myrs; Sdrolias and Müller, 2006). In addition, the migration of magmatism, basin dynamics and tectonic evolution show that most of the Andes experienced a phase of flat-subduction (Ramos & Folguera, 2009). These characteristics define the Andean-type orogeny that has been linked to the low-angle subduction of a relatively young oceanic plate (Capitanio et al., 2011). Along-strike variations in orogenic belt thickness and mean elevation as well as shortening rate and timing of deformation imply complex tectonic processes linked to the existence of inherited crustal structures (Giambiagi et al., 2015; Mardones et al., 2021; Mcquarrie, 2002; Riesner et al., 2018).

In this area, the main geological units consist of the Frontal Cordillera to the east, composed of Permian-Triassic eruptive rocks, intruded granitoids, late Paleozoic sequences, and Proterozoic metamorphic rocks. To the west, the transition to the Principal Cordillera is characterized by the presence of highly deformed Mesozoic sequences forming the Aconcagua fold-and-thrust belt. The Principal Cordillera exhibits the Cenozoic volcano-sedimentary rocks of the Abanico and Farellones formations overlooking the Central Depression, filled with Quaternary deposits from the Maipo and Mapocho rivers. The Central Depression marks the transition to the Coastal Cordillera, a Paleozoic-Triassic basement intruded by Jurassic-Cretacous intra-arc sequences (Charrier et al., 2005; Farias et al., 2010; Giambiagi et al., 2003, 2015; Riesner et al., 2018). Total crustal shortening accommodated by the Principal Cordillera and the Frontal Cordillera has been evaluated between 30 and 70 km with the beginning of the deformation starting between 16 and 22 Ma (Giambiagi et al., 2015; Riesner et al., 2019).

Structural features of the eastern piedmont of the Andean Cordillera in the south-central Andes produced destructive earthquakes along active thrust faults in historical times such as the 1861 Mendoza (M ∼ 7) earthquake (Mingorance, 2006). Paleoseismic studies conducted in the western piedmont of the Principal Cordillera, at

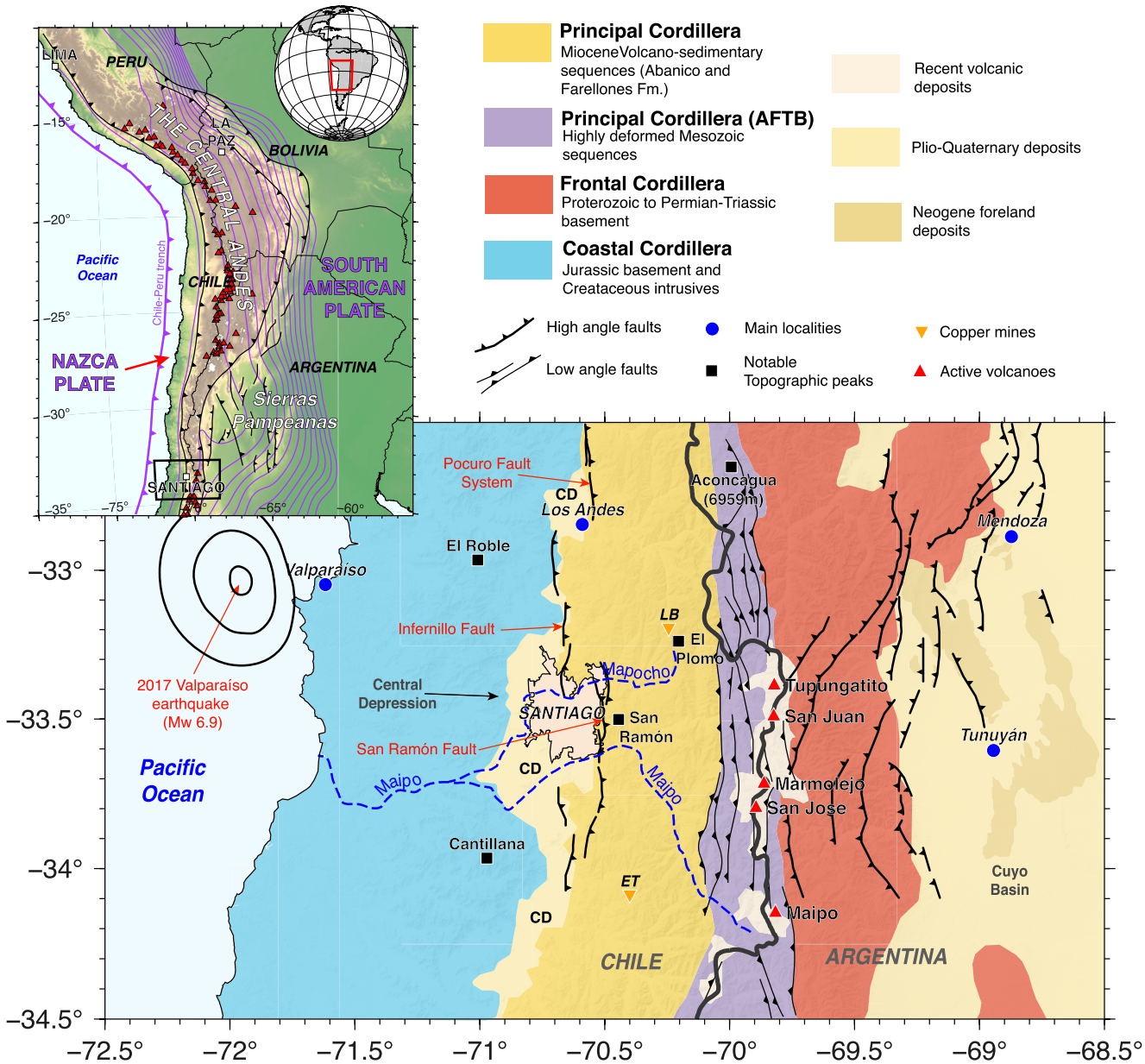

Figure 1. Geological setting of the south-central Andes, between 32.5°S and 34.5°S. The inset (top-left) shows the location of our study region in relation to the western margin of South America, between central Chile and Western Argentina. The red arrow shows the general convergence of the Nazca plate. The purple lines show the Nazca top contours according to the Slab2 model (Hayes, 2018). Convergence velocity is 65 mm/yr (DeMets et al., 2010). Red triangles show the location of active volcanoes along the South-American margin (GVP, 2022). Geological information on the map (bottom) has been compiled from previous studies (Charrier et al., 2005; Farias et al., 2010; Giambiagi et al., 2003; Riesner et al., 2018). The black contours represent the slip area associated with the 2017 Valparaíso earthquake (Ruiz et al., 2017). The thick black line corresponds to the Chile-Argentina border. Note how the principal structures switch from an eastern vergence (Frontal Cordillera and AFTB) to a western vergence (Principal Cordillera). AFTB, Aconcagua fold-and-thrust belt.

~33.5°S, evidenced the occurrence of at least 2 large magnitude (Mw ~7.2–7.5) events, respectively at 17 and 8 ka (Vargas et al., 2014). These events are linked to the activation of the San Ramón thrust fault, a major structure responsible for the uplift of the western Principal Cordillera (Armijo et al., 2010; Charrier et al., 2005; Riesner et al., 2017).

In our study area (Figures 1 and 2), a series of models have been proposed for the general tectonic evolution of the Andes. These conceptual models emphasize the role of crustal thickening of an asymmetric orogenic wedge in which the deformation begins with the uplift of the Principal Cordillera at ~20 Ma and progresses toward the east

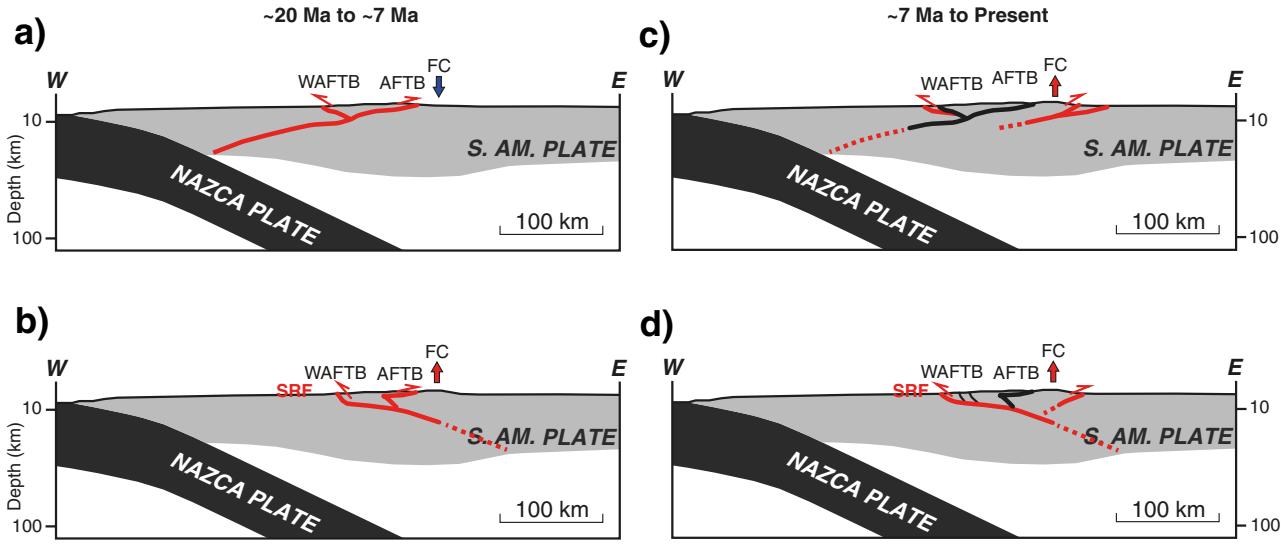

Figure 2. The two principal conceptual models describing the tectonic evolution of the south-central Andes derived from Armijo et al. (2010), Giambiagi et al. (2015) and Riesner et al. (2018, 2019). (a–b) East-vergent (top) versus west-vergent (bottom) models during the Miocene (20-7 Ma). The red lines schematize the presence of active faults. The arrows indicate uplift (red) and/or subsidence (blue) (Riesner et al., 2019). (c–d) Similar as before but now showing the configuration for the Plio-Quaternary (7 Ma to present). Black lines mark the structures no longer active (Armijo et al., 2010; Giambiagi et al., 2015; Riesner et al., 2018, 2019). FC, Frontal Cordillera; AFTB, Aconcagua fold and thrust belt; WAFTB, West Andean Fold and Thrust belt; SRF, San Ramón fault.

(Figures 2a and 2c; Giambiagi et al., 2014; Hilley et al., 2004). These models have been challenged by an opposite hypothesis in which the deformation of the Andes would be controlled by trench parallel, west-vergent structures marked by a westward progression of the main Andean thrust (Figures 2b and 2d). First proposed by Armijo et al. (2010), the timing of deformation for this model has been recently reevaluated based on sediment provenance observations inferring the early uplift of the Frontal Cordillera (Riesner et al., 2018, 2019). Because crustal seismicity is not well known, these tectonic models are mostly based on surface (structural and geochronological) observations. The improved seismicity catalog obtained in this study should help future tectonic models to better constrain the geometry of the structures accommodating crustal deformation in the South-Central Andes.

3. Data and Methods

Our local earthquake tomography is based on the inversion of compressional (P) and shear (S) waves travel times produced by local earthquakes and recorded by both permanent and temporary arrays in central Chile. The main contribution comes from 25 broadband stations deployed in our study area between 2013 and 2017, which are part of the Chilean Seismological Center (CSN) permanent network (Figure 3a). We also use travel-time data obtained during the CHASE temporary experiment: 50 seismometers deployed in the Chilean forearc (Figure 3a), from November 2005 to March 2006 (Marot et al., 2013).

3.1. Unsupervised Earthquake Detection

We first analyzed 4.4 years (1 January 2017 to 31 May 2021) of continuous waveforms recorded by the CSN using PhaseNet (Zhu & Beroza, 2019), a deep learning approach that automatically detects and picks seismic wave arrivals from local earthquakes. This method uses a deep neural network (DNN) model previously trained with a set of ~790,000 manually picked seismic wave arrivals to identify P- and S-phases from three-component seismograms. The outputs are probability density functions of P and S-waves estimated for each seismic station. Using this approach, ~11,780,000 picks were obtained (6,140,699 P phases and 5,635,990 S phases, respectively). The average number of picks per station is 452,950 with a maximum value obtained at station VA01 and a minimum at station MT13 (2,279,648 and 142,464 phases respectively). Station VA01 is located very close to the 2017 (Mw 6.9) Valparaíso earthquake (Ruiz et al., 2017, Figures 1 and 3a), which could explain the much larger number of picks.

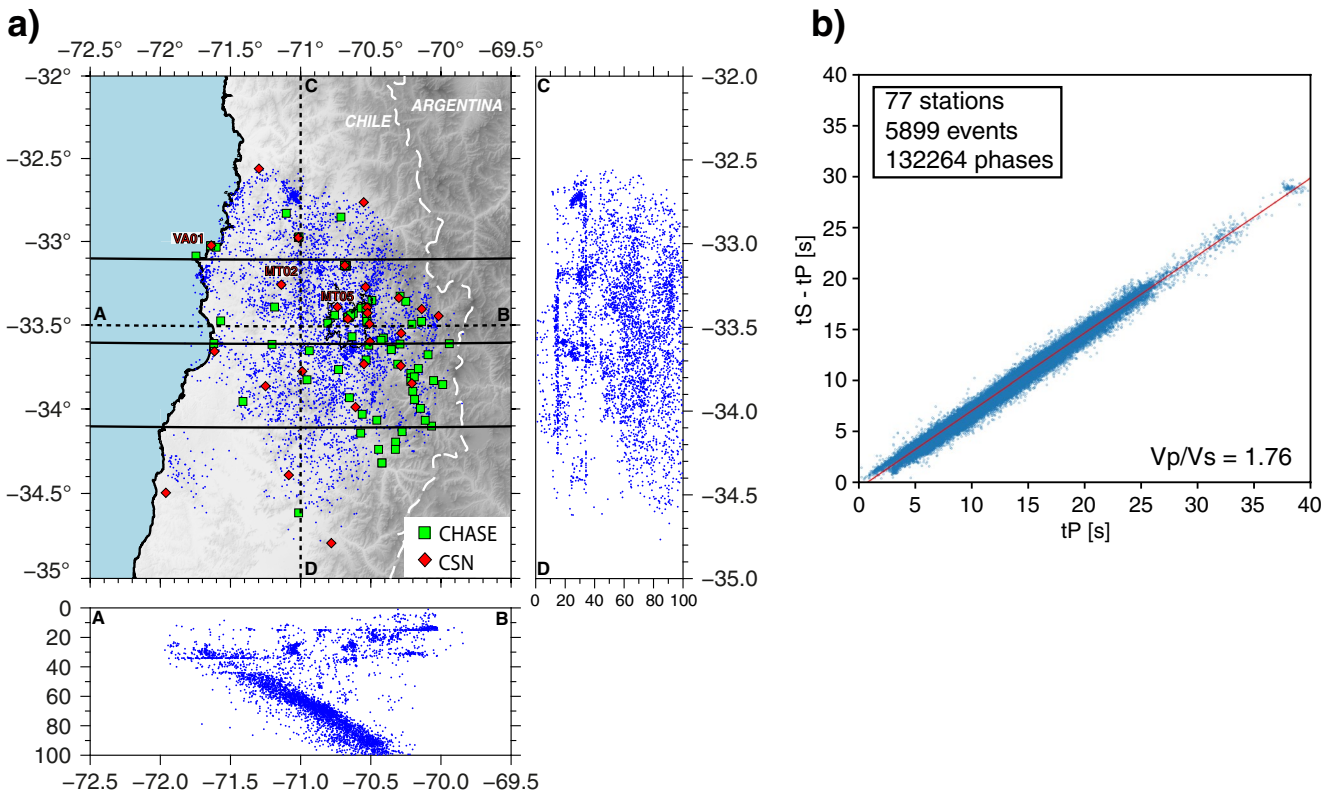

Figure 3. (a) Map of our study area showing seismic stations as well as the epicentral of all the earthquakes selected for the P- and S-wave travel time tomography (see main text). The seismicity is also represented along two cross sections (black dashed lines AB and CD) to better show its depth distribution. Solid black lines mark the location of the cross sections shown in Figure 5. Green squares show the location of the CHASE temporary array (Marot et al., 2013, 2014). Red diamonds correspond to stations from the Chilean seismic permanent network (Barrientos & National Seismological Center (CSN) Team, 2018). (b) Wadati diagram showing S-P time versus P-arrival time for the earthquakes retained for the tomographic inversion. The red line shows the best linear fit with a regression coefficient $R2 = 0.99$ and a slope $Vp/Vs = 1.76$.

The DNN model performs well in identifying phases corresponding to very small events. However, it is important to evaluate if these phases are consistent across the seismic array (Figure 3a) in order to associate them to seismic events. Here, we use a grid-search method in which theoretical travel-times for arbitrary sources are systematically compared with phases previously picked by the DNN model (Zhang et al., 2019). P and S travel time tables are pre-calculated using a simple 1-D velocity model (Figure S1 in Supporting Information S1) for meshes of 0.025° and 1 km, respectively in the horizontal and vertical directions. To reduce the number of false positives, only events with a minimum of five P phases and four S phases are associated. A time window around the theoretical arrival time is used to overcome the inaccuracies of the velocity model. This step resulted in the detection of ~17,000 events.

Between January 2017 and November 2020, 721 events detected and characterized by the CSN also appear in our catalog, which represents ~50% of the CSN catalog for this period. For matching events, average differences in latitude, longitude, and depth are 0.01° ($\sigma = 0.010°$), 0.02° ($\sigma = 0.013°$) and 1.81 km ($\sigma = 1.95$), respectively. The average number of phases per event is 29 and 34 for PhaseNet and the CSN events, respectively.

Several reasons can explain this relatively low number. To build their catalog, the CSN uses a higher number of stations (hence the higher number of phases) while we only use a selection of closeby stations to avoid the picking of refracted phases for which PhaseNet was not trained (Zhu & Beroza, 2019). The other reason could be the grid extent used for the phase association (Zhang et al., 2019). In this study, we only search for events with hypocentrals distances shorter than 150 km. On the other hand, the CSN analyzes events occurring at much greater distances, including deep events within the subducting Nazca slab.

We also compared our catalog with the one obtained by Ammirati et al. (2019). About 90% (953 events between January 2021 and March 2019) of the events from Ammirati et al.'s (2019) catalog also appear in our catalog. In

this case, the average location differences are 0.01° ($\sigma = 0.006°$), 0.01° ($\sigma = 0.009°$) and 1.01 km ($\sigma = 1.19$ km), respectively in latitude, longitude, and depth. Our catalog has a slightly higher average number of phases compared to Ammirati et al.'s (2019) catalog (23 and 19 phases, respectively). In both studies, the seismic network configuration (Figure 3a) is similar, which can explain the higher number of matching events.

3.2. Phase Picking Validation

The accuracy of the automated phase picking algorithm used in this work can be evaluated by comparing the obtained phases with those obtained manually (Figure 4, Table S1 in Supporting Information S1). In this section, we do such a comparison with phases picked by the CSN analysts between January 2017 and November 2020 and also with the phases obtained by Ammirati et al. (2019), between January 2017 and March 2019. We show this comparison for phases picked at two particular stations: MT02 and MT05 (Figure 3a). The former is located in a mountainous environment, far from any source of anthropogenic noise. The latter is located in northwestern Santiago and thus presents a high level of noise (Figure S2 in Supporting Information S1).

In general, we observe that the residuals;

$$r = t_{\text{PhaseNet}} - t_{\text{manual}}$$

(where t_{PhaseNet} and t_{manual} are absolute times associated with PhaseNet and manual phase picking, respectively) are mostly smaller than 0.5 s and centered on 0 s. This is especially true for P-waves observed at station MT02 (Figure 4). CSN picks residuals tend to degrade at stations MT05 in particular for S-waves. The dispersion of residuals is higher (although mostly <1 s). We also note that for the CSN picks, the distribution of residuals is not symmetrical and most residuals are between 0 and 1 s. This indicates a systematic delay between PhaseNet and CSN picks (either PhaseNet picks late or the CSN analysts pick too early). The comparison with Ammirati et al.'s (2019) phases at station MT02 shows low residuals ($r < \sim 0.25$ s) for both P- and S-waves. At station MT05, residuals remain low (slightly higher for S-waves) and centered on 0 s. This observation thus suggests that the CSN analysts tend to pick too early. Average residuals and associated standard deviation for all stations are summarized in Table S1 in Supporting Information S1.

The entire earthquake dataset was first located using the aforementioned 1D initial velocity model (Figures 3a and S1 in Supporting Information S1). The phase quality for these events can be further assessed by plotting a Wadati diagram (Figure 3b). This diagram is very useful to evaluate the phase association process as any point not fitting well with the linear relationship might correspond to phases incorrectly identified either by not being associated to the right event or by being of the wrong type.

The central region of Chile is characterized by an important mining activity, with two of the world largest copper mines, Los Bronces and El Teniente, located within our study area (Figure 1). These sites, in particular, Los Bronces, which is of open-pit type, seem to produce an important seismicity. To discriminate such mining events from earthquakes of tectonic origins, we binned the origin time of events located close to these mining sites according to hour of the day (Figure S3 in Supporting Information S1) and observed that most of these events show a timing pattern. This observation is particularly well-observed for the Los Bronces mine with origin times preferentially distributed around 17:00–18:00 and 20:00–21:00 UTC. We used this information to discard the events suspected of being mining explosions from the subsequent tomography.

3.3. Local Earthquake Tomography

Once our quality control was completed, we selected earthquakes with a preliminary 1-D location obtained with 8 or more P-wave arrival times, 4 or more S arrival times, a focal depth of less than 150 km, and an azimuthal gap smaller than 200°. This resulted in a dataset of 5,899 earthquakes with 74,619 P arrival times and 57,635 S arrival times recorded at 77 seismic stations (Figure 3a). About 90% of these phases were automatically detected by PhaseNet. The remaining 10% come from the CHASE dataset.

All earthquakes and stations are contained within a rectangular region of 270 × 324 km in longitude and latitude, respectively, extending from 4 km above sea level to 152 km depth. All the rays are traced from the source to the receiver without the need for elevation corrections. The size of the model region allows us to use a flat-Earth approximation. Geographical coordinates are converted to cartesian coordinates, and all the computations

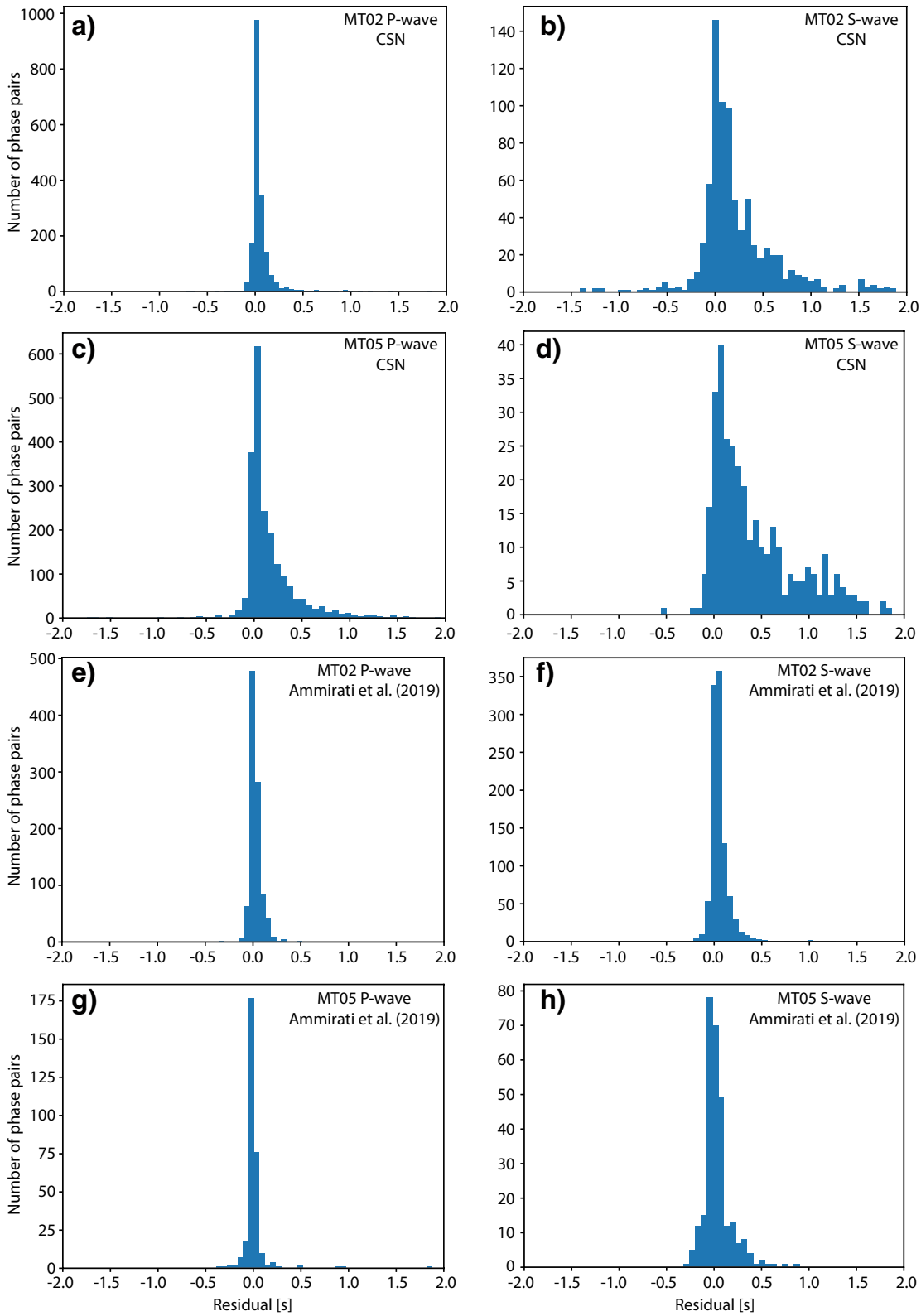

Figure 4. (a–d) diagram showing the time difference between PhaseNet picks obtained in this work and manual picks obtained by the CSN. The comparison is made for both P and S phases obtained at two stations: MT02 and MT05 (see Figure 3 for corresponding locations). The observation period extends from JAN 2017 to NOV 2020. (e–h) Same as before except this time the comparison is made for picks obtained by PhaseNet and manual picks obtained by Ammirati et al. (2019). In this case the period of observation is JAN 2017–MAR 2019.

are done in a cartesian grid. Travel times are calculated using the finite difference method of Podvin and Lecomte (1991), using a grid spacing of 0.5 km in the x, y, and z directions (longitude, latitude, and depth, respectively). This method is well suited for computing travel times in media with large lateral velocity perturbations. The P- and S-wave velocity models are parameterized in terms of $6 \times 6 \times 3$ km constant velocity cells, resulting in $45 \times 54 \times 52$ cells in the x, y, and z directions, respectively.

The inversion is performed simultaneously for P- and S-waves following the method of Benz et al. (1996) as modified by Tryggvason et al. (2002) to include S-wave arrival times. This method first linearizes the non-linear tomographic problem and then iteratively performs the joint inversion for velocity structure and earthquake relocations (e.g., Spencer & Gubbins, 1980). A penalty on the cross-gradient of the *Vp* and *Vs* models has been added in the cost function, to get a more robust reconstruction of the *Vp*/*Vs* ratio. The initial model used for the iterative inversion is the same 1-D model used for phase association and preliminary earthquake location (Figure S1 in Supporting Infomartion S1). Velocity changes from this reference model are solved using the iterative LSQR (least-square) method described in Paige and Saunders (1982). A smoothing constraint is applied to control the model roughness (Benz et al., 1996). After testing values ranging from 200 (overdamped) to 10 (underdamped), we found that a smoothing parameter of $k = 50$ produces the best variance reduction without degrading the appearance of the models. After 10 iterations the RMS of the P- and S- wave residuals did not decrease significantly. The initial RMS of the P wave arrival times was 0.59 s, and the value after 10 iterations was 0.22 s. For S-wave arrival times, the initial RMS was 0.87 s and the final one 0.22 s.

To reduce the effect that the parameterization in terms of constant velocity cells could have in small velocity anomalies, we apply an offset-and average interpolation in the two horizontal and in the vertical dimensions. This is accomplished by shifting the model origin by 0, 1/3, and 2/3 of the dimensions of the cell in each dimension. The resulting 27 ($3 \times 3 \times 3$) realizations of the tomographic inversion are then averaged on a finer grid of $2 \times 2 \times 1$ km, which is the one shown in Figures 5 and 6. The checkerboard reconstruction (Figures S4 and S5 in Supporting Information S1) is obtained following the same methodology.

3.4. Earthquake Location Procedure

The 3D tomographic model is parameterized in a grid of $135 \times 162 \times 156$ nodes with a 2 km spacing along both longitudinal and latitudinal directions and 1 km along the vertical direction. We use the aforementioned finite-difference ray-tracing method (Podvin and Lecomte, 1991) to calculate source-station travel-times corresponding in the 3-D model, to be used for subsequent non-linear, 3-D probabilistic earthquake locations (Lomax et al., 2000). As this step requires cubic meshes, velocities in the model are interpolated every 2 km along the vertical direction. The non-linear approach for the seismic location (NonLinLoc) is based on the probabilistic reformulation of the inverse problem (Tarantola & Valette, 1982) where a Gaussian error is used for the source parameters (hypocentral coordinates and origin time) and the observed travel-times (Lomax et al., 2000). The resulting hypocenter location is represented by a probability density function. We relocated the ~17,100 events from the PhaseNet catalog within our 3D tomographic model. Some phases picked by the DNN model correspond to false positives and/or are only visible on a small number of stations. However, these false positives are easy to identify by their poorly constrained hypocenter locations after phase association. We only kept in our catalog the events with RMS (residual mean square) lower than 0.3 s and hypocenter location uncertainties lower than 10 km in both vertical and horizontal directions. These restricting parameters yielded a total of 13,969 hypocenters corresponding to seismic events that occurred between 1 January 2017 and 31 May 2021 (Figure 7). Local magnitude (ML) was estimated based on S-wave maximum amplitude using the following equation (also used by the CSN to estimate local magnitude of earthquakes occurring in Central Chile):

$$M_l = \frac{1}{n}\sum_{i=1}^{n}[\log(A) + 0.42 \times \log(r) + 0.005 \times r - 1.35]_i$$

for which, A is the S-wave maximum amplitude (nm/s), r is the hypocentral distance (km), n is the number of stations.

In addition, when two earthquakes are very close to each other, the source–receiver distance is much larger than the physical separation between them and the source-receiver ray paths are almost identical. It is thus possible to minimize the residual between observed and calculated travel-time difference (or double-difference) between

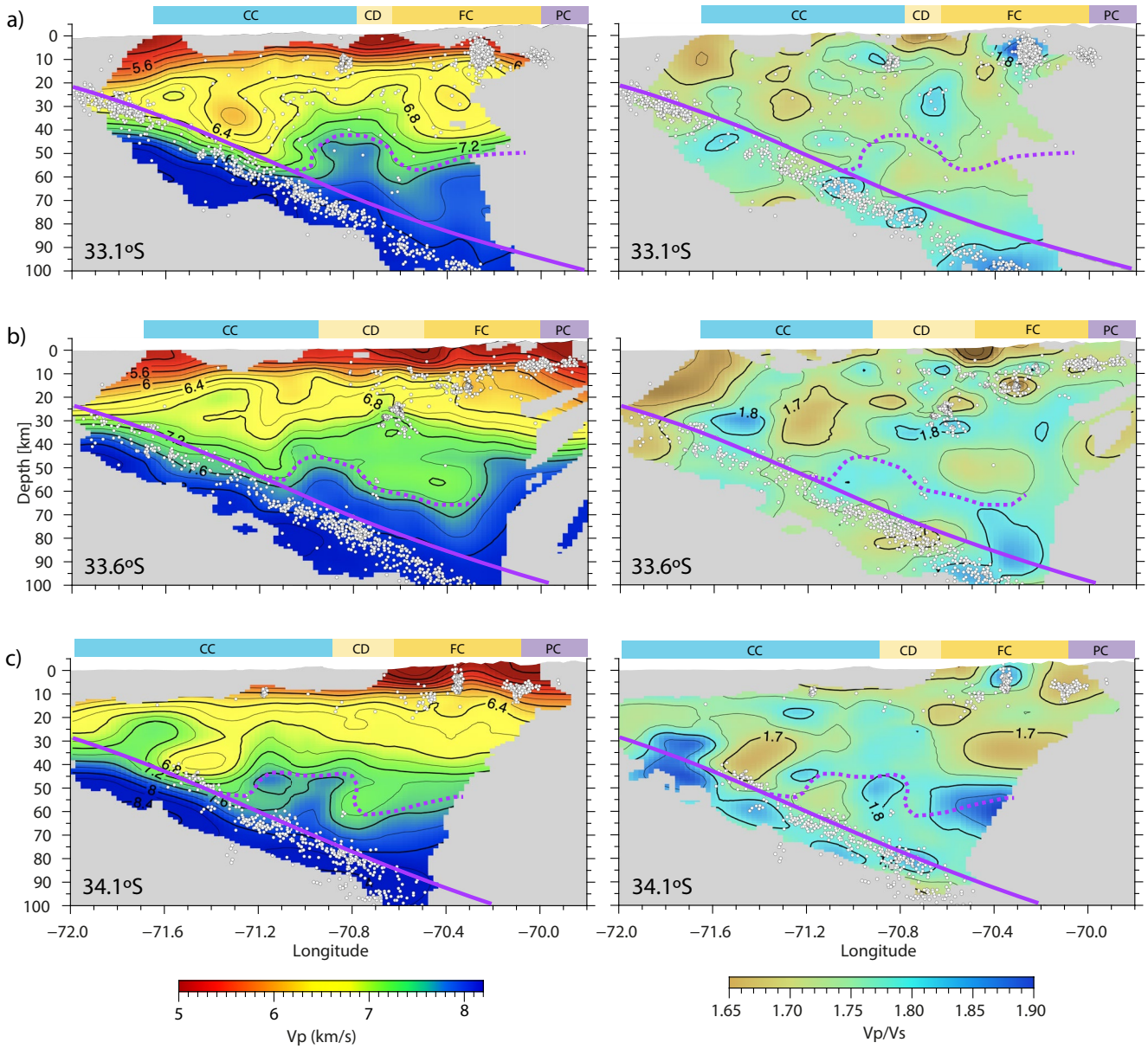

Figure 5. Travel time tomography results. The cross sections (a–c) depict the compressional-wave (*Vp*) velocity and compressional/shear-wave (*Vp*/*Vs*) ratio variations through our tomographic model. The white dots correspond to the projection (with a swath width of 0.2°) of 3-D locations obtained in this work (see Figure 7). The purple solid line shows the top of the slab according to the Slab2 model (Hayes, 2018). The purple dashed line materializes the *Vp* = 7.5 km/s, interpreted as the seismic Moho (see main text). The location of the cross sections is shown in Figure 3. For each cross section, letters at the top refer to the geological units described in Figure 1 (CC, Coastal Cordillera; CD, Central Depression; FC, Frontal Cordillera; PC, Principal Cordillera).

these two events recorded at a common station by slightly adjusting the relative positions of their hypocenters and origin times, reducing uncertainties associated with P and S phases (Waldhauser & Ellsworth, 2000). This double-difference technique proved to be very useful to better highlight tectonic structures by "gathering" the events sharing a similar source mechanism along these structures. Here, we relocated a selection of earthquakes beneath the Central Depression and Principal Cordillera (located between 71°S and 69.5°S with focal depths ranging from 0 to 40 km) with the double-difference method in order to refine the potential alignment of seismicity along tectonic structures in this particular area of interest (Figures 1 and 2). Only pairs of events separated by less than 5 km (probabilistic 3D locations) are considered for double-difference relocations. This step uses the 1-D velocity model used for phase association and preliminary locations (Figure S1 in Supporting Information S1).

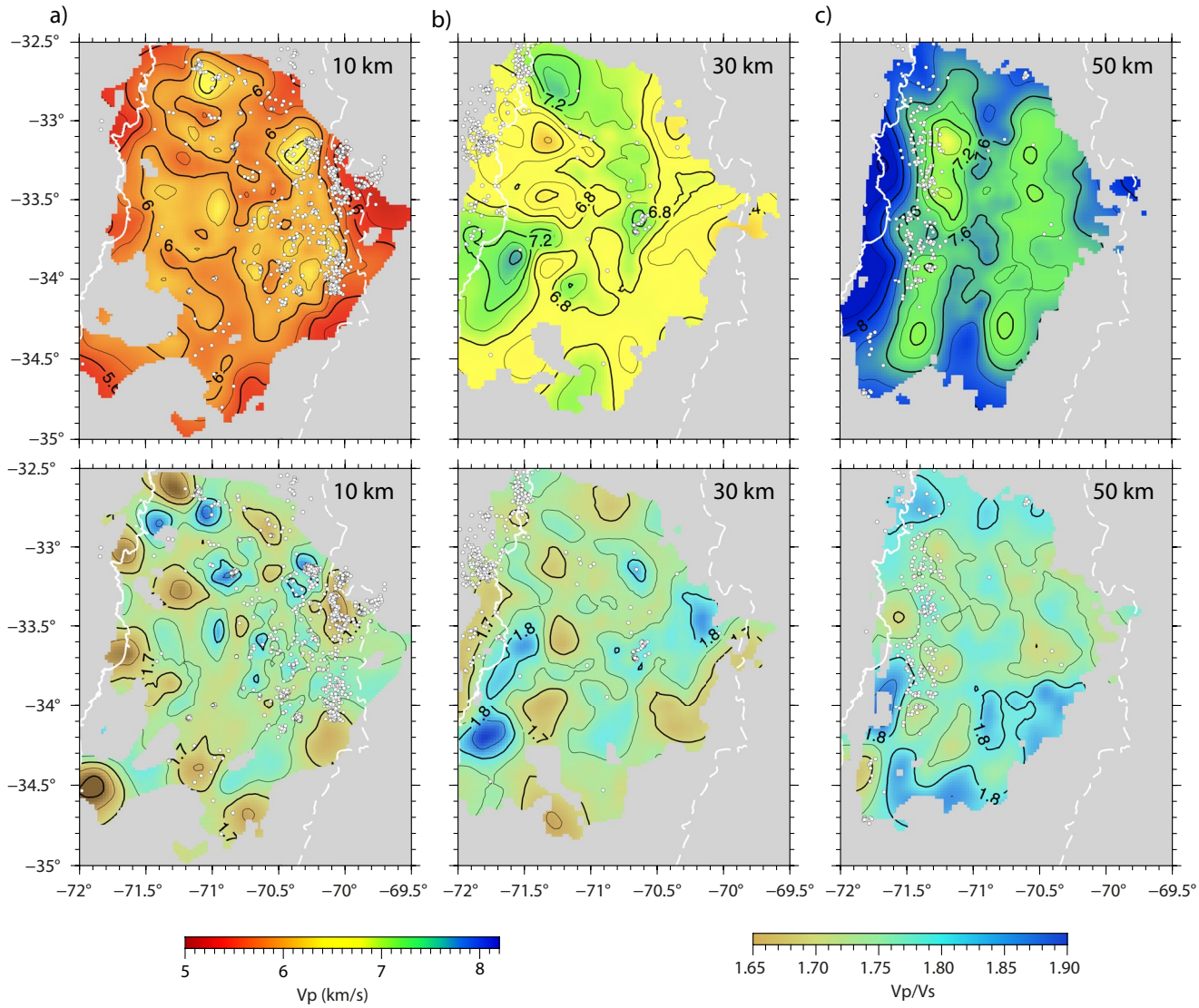

Figure 6. Map slices (a–c) showing the compressional-wave (*Vp*) velocity and compressional/shear-wave (*Vp*/*Vs*) ratio variations at 10, 30, and 50 km, respectively. The white dots correspond to the projection of 3-D locations (within the respective depth range) obtained in this work (see Figure 7). The solid white line corresponds to the Chilean coast. The dashed white line marks the Chile–Argentina border.

Finally, we selected crustal events with local magnitude greater than ML > 3.0 to compute their moment tensor using a modified version of the ISOlated Asperities code (ISOLA; Sokos & Zahradnik, 2008; Vackář et al., 2017). This technique consists in optimizing the variance reduction between observed and synthetic regional, three-components broadband waveforms. The synthetics are obtained by varying the moment tensor parameters and convolving the corresponding source function with precalculated Green's functions (Figures S6–S12 in Supporting Information S1). For each event, the corresponding NS, EW, and Vertical records are first corrected from instrumental response and filtered between 0.02 and 0.12 Hz. The velocity model used to compute the Green's function is the aforementioned 1-D model (Figure S1 in Supporting Information S1).

4. Results

4.1. Crustal Velocity Variations

Although the number of stations is limited and their spacing is rather large (~20 km on average), the amount of events used for the tomographic inversion produced images (Figures 5 and 6, S13–S15 in Supporting

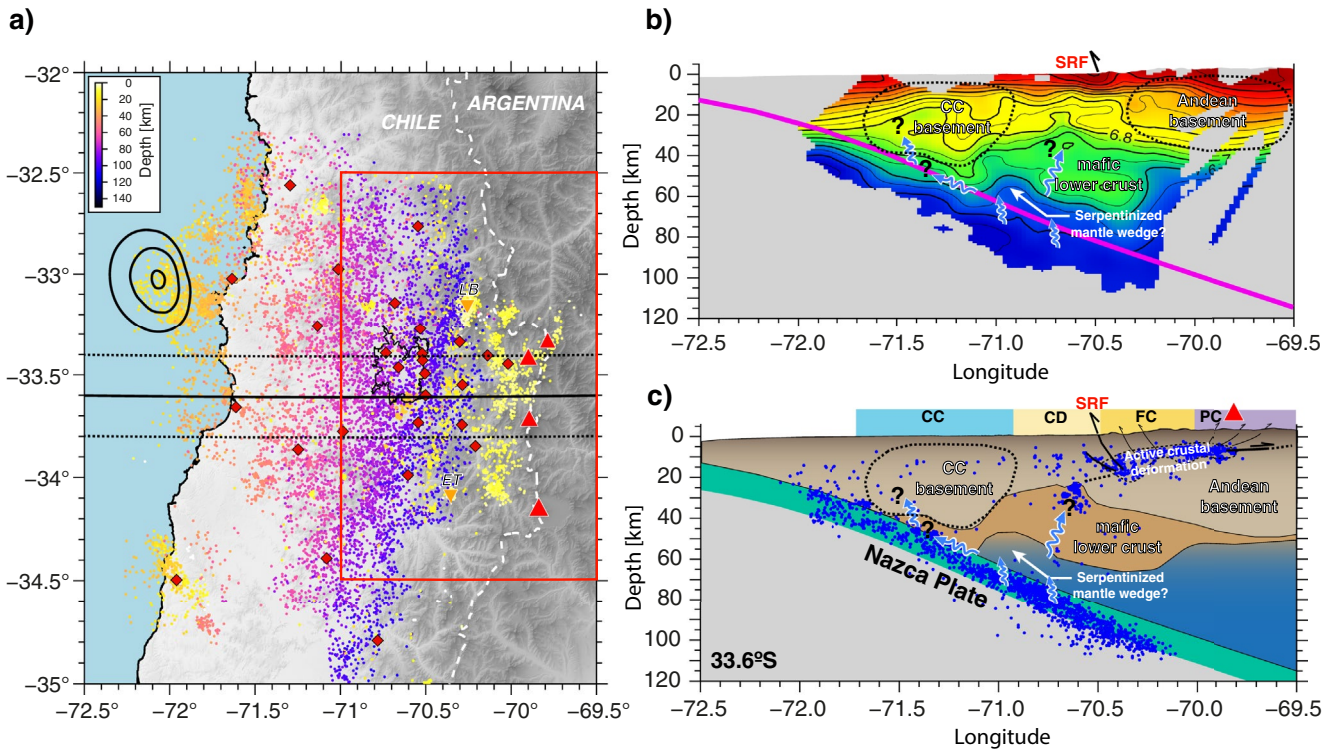

Figure 7. (a) Map showing the epicentral distribution of 13,969 local earthquakes detected by the deep neural network model (PhaseNet) and located within our 3-D model (see details in the main text). The hypocenters are color-coded by focal depth. The solid black lines show the location of the cross section (b) and (c). The two dashed black lines represent the swath for which the seismicity is projected. The red rectangle delimits the West Andean Thrust area (Figure 8). The red diamonds mark the location of the permanent Chilean seismological network (Barrientos & National Seismological Center (CSN) Team, 2018, Figure 3) and correspond to the stations used in this study. The black polygon corresponds to the city limit of the city of Santiago. Black contours mark the slip area associated with the 2017 Valparaíso earthquake (Ruiz et al., 2017, Figure 1). (b) Cross section across the tomographic model at 33.6°S (same as Figure 5b) with interpretations (see the discussion in the main text). The purple solid line shows the top of the slab according to the Slab2 model (Hayes, 2018). Blue wiggling arrows symbolize potential fluid migrations. (c) Schematic lithospheric section based on the velocity variations (Figures 5 and 6) and the seismicity catalog obtained in this work. Interpretations are similar to (b). Letters at the top of each cross section refer to the geological units described in Figure 1 (CC, Coastal Cordillera; CD, Central Depression; FC, Frontal Cordillera; PC, Principal Cordillera). The red triangle shows the approximate location of the volcanic arc (Figure 1).

Information S1) exhibiting an improved level of details compared to previous studies (Farias et al., 2010; Marot et al., 2014).

The velocities observed in the first 10 km vary within the 4.8–6 km/s and 3–3.4 km/s ranges for *Vp* and *Vs*, respectively (Figures 5, 6, and S16 in Supporting Information S1). In the western part of our study region, the low ray densities (Figure S15 in Supporting Information S1) limit the spatial resolution at shallow depths. The corresponding *Vp*/*Vs* ratio beneath the Principal Cordillera appears varying and locally alternates between values lower than $Vp/Vs < 1.7$ and greater than $Vp/Vs > 1.8$. Relatively higher values of *Vp*/*Vs* ratio are observed at ~10 km beneath the Central Depression (~70.6°S) and in the Principal Cordillera (~70.4°S). Interestingly, at ~33.5° (Figure 5b), an abnormally low value of the *Vp*/*Vs* ratio (<1.65) is observed at shallow depths (0–5 km). This feature geometrically coincides with the scarp of the San Ramón fault (Figure 1; Ammirati et al., 2019; Armijo et al., 2010; Charrier, 2005; Vargas et al., 2014).

At deeper levels, in the 10–30 km depth range (Figure 5), crustal P-wave velocities increase from 6 to ~6.8 km/s (3.4–~3.8 km/s for *Vs*, Figure S16 in Supporting Information S1) with a *Vp*/*Vs* ratio of about 1.75. Beneath the Central Depression (~70.8°W) velocities locally increase to higher values (*Vp* ~7 km/s, *Vs* ~3.9, and *Vp*/*Vs* ~ 1.8) *Vp*/*Vs* ratio. Our images also show a zone of relatively high crustal *Vp* and high Vp/*Vs* ratio ($Vp > 6.8$ km/s and *Vp*/*Vs* ~1.8), located on the westernmost side of our study region, at 30 km depth (Figures 5b, 5c and 6b). Beneath the Coastal Cordillera (Figures 5 and 6b), crustal velocities are relatively low (~6.5 km/s)

In general, we observe that lower crustal velocities (depths > 30 km) vary from ~6.8 to 7 km/s (*Vp*) and velocities observed for depth >50–60 km are greater than *Vp* ~ 8 km/s.

4.2. Crustal Seismicity

The seismicity distribution is affected by the geometry of our seismic network. For example, no earthquakes are observed in the Argentine cordillera and back arc region farther east, owing to a lack of nearby stations.

Location errors are estimated from the 68% confidence ellipsoid (computed from the location probability density function). Our final 3-D probabilistic locations are characterized by an average horizontal error of 3.6 km with a standard deviation of σ = 1.8 km, and a vertical error of 3.8 km (σ = 1.6 km). Average residuals between observed and modeled phases are low with a RMS of 0.16 s (σ = 0.05 s). The average number of phases used for the locations is 18 ± 7.

About 35% of the events in the catalog corresponds to crustal earthquakes with hypocenter locations beneath the Principal Cordillera and Central Depression (Figures 1 and 7). Because the seismic network in this area is denser, the hypocentral locations are better constrained with location errors of 2.4 km (σ = 1.3 km) and 3.2 km (σ = 1.4 km) in the horizontal and vertical directions, respectively. The RMS for this selection of crustal earthquakes is 0.15 s (σ = 0.06 s), on average. Local magnitude (ML) estimation (Fig. S17) indicates that our catalog is complete for earthquakes with magnitudes ML ∼ 1.5 and above.

Double-difference hypocenter relocation (Waldhauser & Ellsworth, 2000) performed on the selection of crustal events (Figures 7a and 8) yielded a total of 4,589 events. The relocated seismicity concentrates along potential tectonic structures or within large clusters (Figure 8). In general, the distribution of crustal earthquakes displays a similar pattern as described in previous studies (Ammirati et al., 2019; Farías et al., 2010). In detail, the seismicity beneath the Principal Cordillera is concentrated along two N-S bands (Figure 8a). The first one extends beneath the Principal Cordillera, between 70.2°W and 69.8°W at a depth of ∼10 km. Directly to the west (∼70.5°W), the second band is mostly characterized by deeper hypocenters with focal depth ranging between 15 and 20 km. As mentioned by Ammirati et al. (2019), the seismicity in this sector follows the scarp of the San Ramón fault (Figures 1 and 8a) at the surface and is likely related to the uplift of the Principal Cordillera (West Andean Thrust; Armijo et al., 2010). However, the increased number of events in this study suggests that the seismicity beneath the Principal Cordillera extends north of 33.2°S, giving further support to the hypothesis of a connection between the San Ramón fault and the Pocuro fault systems (Armijo et al., 2010; Charrier et al., 2005).

Focal mechanisms obtained in this work correspond to seven crustal earthquakes located beneath the Frontal Cordillera and the Principal Cordillera (Table 1). Their corresponding magnitudes range between 3.4 and 4.8. Six of these solutions are located within the band of seismicity located beneath the Principal Cordillera and one is located beneath the Frontal Cordillera (Figure 8a). Fault plane solutions mostly characterize strike-slip (right-lateral) and reverse events.

Our results also highlight the presence of clustered seismicity (Figures 7 and 8). In particular, we observe a concentration of earthquakes ∼30 km beneath the metropolitan area of Santiago at 33.6°S; 70.7°W (C1 in Figures 7c, 8a, and 8d). Two other seismicity clusters are also observed around 33.2°S; 70.3°W (C2 in Figures 7b, 8a, and 8b) and ∼34.1°S; 70.4°W (C3 in Figures 7d, 8a, and 8f) at depths of ∼10 and ∼5 km, respectively. As mentioned before, clusters C2 and C3 match the location of the Los Bronces and El teniente copper mines (Figures 1, 7 and 8) and probably correspond to mislocated explosions. Another important concentration of seismic events (C4 in Figures 8a and 8b) can be observed around 33.2°S and 70°W, beneath the Chile–Argentina border.

5. Discussion

5.1. Crustal Velocity Structure

The relatively low crustal velocities observed between 0 and 10 km (Figures 5 and 6) are comparable with average velocities measured in other continental upper crusts (Christensen & Mooney, 1995; Brocher, 2005). The lowest velocities (Vp < 5 km/s) are observed beneath the Central Depression and the West Andean Thrust (Figure 5). Such velocities generally indicate the presence of sedimentary rocks, which in this case could correspond to the Quaternary deposits filling the Central Depression and the sediments of the Miocene Abanico basin. Compressional velocities between 5 and 6 km/s rather indicate the presence of felsic rocks such as andesites, which mainly characterize the Principal Cordillera (Charrier et al., 2005; Thiele, 1980). Although our model lacks resolution at shallow depths, beneath the CC, the observed velocities of Vp ∼5.5 km/s and Vs ∼3.3 are compatible with the presence of Mesozoic altered felsic intrusive as described in Charrier et al. (2005) and Farias et al. (2010).

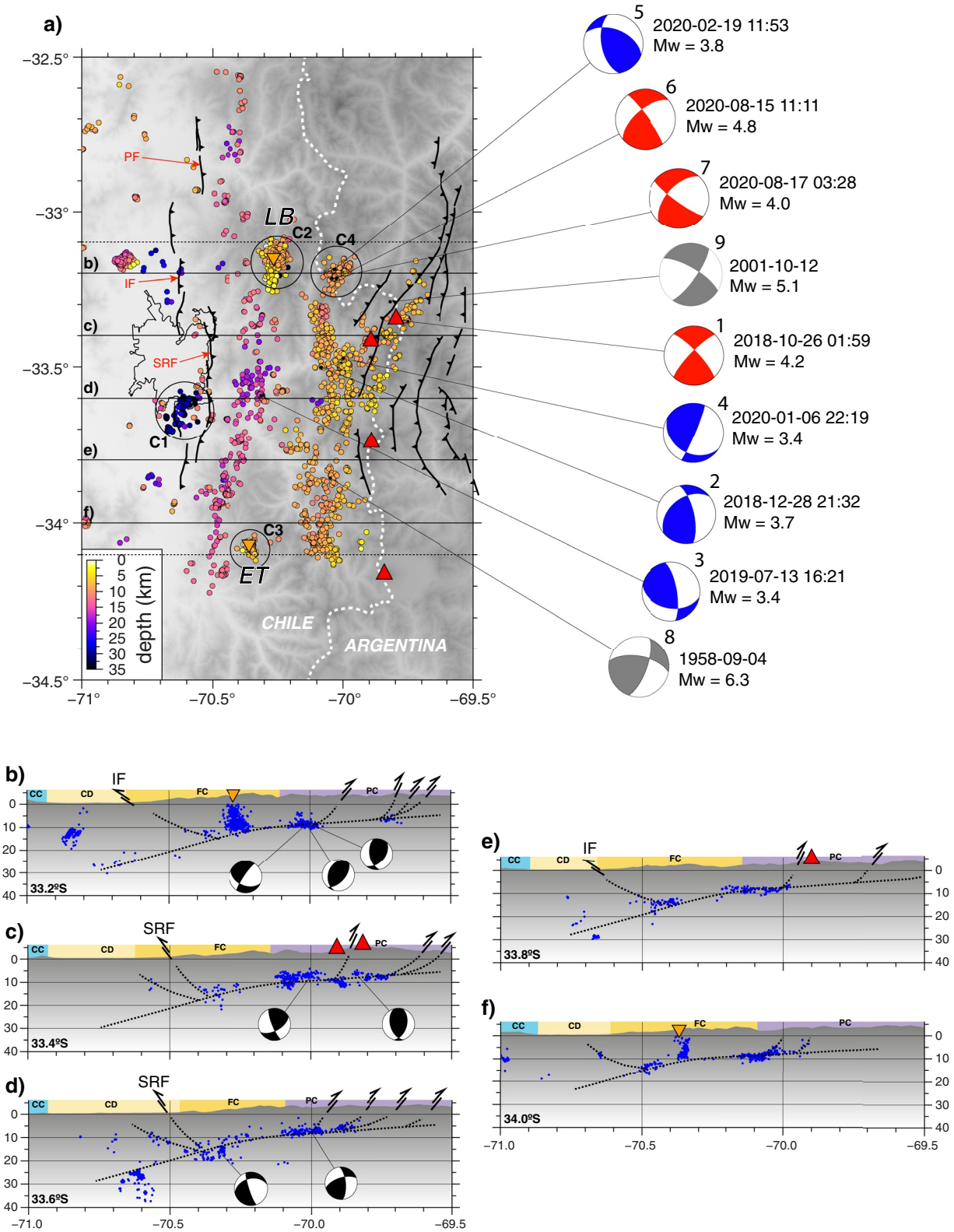
a)
−32.5°
−33°
−33.5°
−34°
−34.5°
−71°
−70.5°
−70°
−69.5°
PF
IF
SRF
LB
C1
C2
C3
C4
ET
CHILE
ARGENTINA
depth (km)
0
5
10
15
20
25
30
35
b)
c)
d)
e)
f)
5 2020-02-19 11:53 Mw = 3.8
6 2020-08-15 11:11 Mw = 4.8
7 2020-08-17 03:28 Mw = 4.0
9 2001-10-12 Mw = 5.1
1 2018-10-26 01:59 Mw = 4.2
4 2020-01-06 22:19 Mw = 3.4
2 2018-12-28 21:32 Mw = 3.7
3 2019-07-13 16:21 Mw = 3.4
8 1958-09-04 Mw = 6.3
CC
CD
FC
PC
IF
SRF
33.2ºS
33.4ºS
33.6ºS
33.8ºS
34.0ºS
−71.0
−70.5
−70.0
−69.5

Figure 8.

Table 1
Regional Moment Tensor Inversion Results

Id	Date	Time	Longitude (°)	Latitude (°)	Depth (km)	Strike (°)	Dip (°)	Rake (°)	Ml	Mw	N Comp.
1	26 October 2018	01:59	−69.75468	−33.35827	8	224	79	168	4.2	4.4	21
2	28 December 2018	21:32	−70.00282	−33.48826	8	23	85	121	3.7	3.7	22
3	13 July 2019	16:21	−70.31853	−33.58715	17	350	72	129	3.4	3.4	12
4	06 January 2020	22:19	−70.04703	−33.51752	9	232	43	148	3.4	3.5	24
5	19 Febraury 2020	11:53	−70.02893	−33.16514	11	292	50	46	3.8	3.8	27
6	15 August 2020	11:11	−70.01468	−33.20950	11	230	62	171	4.7	4.8	27
7	17 August 2020	03:28	−70.03723	−33.21845	9	222	57	−169	3.8	4	27
8*	04 September 1958	09:26	−70.14	−33.826	8–10	280	62	157	-	6.3	-
9**	12 Otober 2001	04:21	−69.815	−33.286	5–10	301	73	−15	-	5.1	-

Note. Id, identification number; Ml, Local magnitude; Mw, moment Magnitude; N, Number of components used in the inversion.

Relatively high values of the *Vp*/*Vs* ratio observed between 0 and 10 km depth (Figure 6a) are linked to local decrease in S-wave velocities (Figure S16 in Supporting Infomartion S1) and can be linked to the presence of hydrous fluids (Watanabe, 1993). Alternatively, these values are also compatible with the presence of basaltic rocks corresponding to local magmatic intrusions (Christensen & Mooney, 1995). Such intrusives were identified in the Coastal Cordillera (Pichowiack, 1994; Farias et al., 2010) and in the Principal Cordillera (Kay et al., 2005). Other zones of high *Vp*/*Vs* ratio are observed beneath the Central Depression at 10 km depth (Figures 5a and 5b) and also in the Principal Cordillera beneath the Los Bronces and El Teniente copper mines. In this context, they could coincide with fluid circulations often linked to large porphyry copper deposits (Mernagh et al., 2020; Nash & Theodore, 1971).

Deeper crustal velocities (10–30 km depths) of ∼6.8 km/s (3.4–∼3.8 km/s for Vs) are in good agreement with the presence of felsic rocks typical of continental crusts at similar depths (Christensen & Mooney, 1995). Such velocities are observed west of 70.8°W and would characterize the Coastal Cordillera basement down to 35–40 km (Figures 5, 6b, and 7).

The higher than average values of crustal seismic velocities observed beneath the Central Depression (∼70.6°W, Figures 5, 6b, and 7) seem to suggest a different nature of the Coastal Cordillera and Principal Cordillera basements. Such high crustal velocities usually indicate the presence of mafic composition, typical of rocks in the greenschist or mafic granulite facies (Brocher, 2005; Christensen & Mooney, 1995). Petrological studies combined with geophysical observations (e.g., Hacker, 1996) demonstrated that the increase of pressure and temperature at increasing depths in the presence of water would favor mineralogical transformations from felsic rocks to mafic rocks. This is interesting because this area of higher velocities is also characterized by a relatively higher *Vp*/*Vs* ratio (∼1.8), which could indicate the presence of hydrous fluids. Above this area, previous studies evidenced the occurrence of late Oligocene-Miocene volcanic activity in the surroundings of Santiago (Thiele, 1980). The isotopic signature of the corresponding volcanic rocks appears to be similar to those found in the current Andean arc (Hildreth & Moorbath, 1988; Vergara et al., 2004) and are characterized by a common subduction-related origin with lower-crustal contamination. For this reason, the higher *Vp*/*Vs* ratio could also be related to local changes in crustal lithologies (such as mafic basaltic intrusives).

The seismic Moho can be defined as the change in seismic wave velocities corresponding to the transition between mafic granulites ($Vp \sim 7.5$ km/s and $Vs \sim 4.2$ km/s) and eclogitic and/or ultramafic lithologies ($Vp > 8$ km/s and $Vs > 4.4$ km/s) characterizing the upper mantle (Christensen & Mooney, 1995; Brocher, 2005). In our model (Figures 5, 6, and S6 in Supporting Information S1) this transition is materialized by the $Vp = 7.5$ km/s and

Figure 8. (a) Map centered on the West Andean Thrust (see location on Figure 7) showing 4589 double-difference relocated hypocenters, color-coded by focal depth. Black solid lines show the location of the cross sections (b)–(f). Beachballs correspond to focal mechanisms described in Table 1. Clear strike-slip mechanisms appear with red quadrants whereas mostly reverse mechanisms appear with blue quadrants. Focal mechanisms with gray quadrants (nº 8 and 9) are from Alvarado et al. (2009) and the GCMT catalog (Ekström et al., 2012), respectively. (b)–(f) Integrated cross sections showing the projected hypocenters and focal mechanisms shown in (a). The swath width is 0.1°. Dotted lines show the structure inferred from the seismicity. Orange inverted triangles show the location of the Los Bronces (LB) and El Teniente (ET) copper mines. Red triangles correspond to active volcanoes (Figure 1).

Vs = 4.2 km/s velocity contours, hence suggesting that the forearc crustal thickness, in our study region, varies between ∼45 and ∼55 km, in good agreement with values estimated from earlier converted phases studies (Fromm et al., 2004; Gilbert et al., 2006).

In our study area, velocity variations at the base of the crust (∼50 km) indicate the presence of relatively low mantle velocities (7.6–7.8 km/s). This feature appears quite consistent in the region illuminated by our tomographic images (Figures 5, 6c, and 7) and makes the crust beneath the Central Depression and the eastern Coastal Cordillera to appear thinner. This observation is consistent with the presence of a serpentinized mantle wedge (Carlson & Miller, 1997, 2003). Interestingly, high crustal velocities and *Vp*/*Vs* ratios ($6.5 < Vp < 6.8$ km between 20 and 30 km depths) are observed at the westernmost side of our study area (west of 71.5°W; Figure 5) above the subduction interface. Such relatively high crustal *Vp* and *Vp*/*Vs* ratio have been observed in the northern Chile subduction zone and have been related to fluid migration from the dehydrating mantle wedge, along the subduction interface (Araya Vargas et al., 2019; Condit et al., 2020; Contreras-Reyes et al., 2021). However, these interpretations were backed up by resistivity data which are unavailable in our study region.

5.2. Architecture of the South-Central Andes

5.2.1. Principal and Frontal Cordillera

The hypocenter located within our improved velocity models (Figures 5–8) suggest that the ongoing crustal deformation observed beneath the Principal Cordillera at ∼33.5°S, could be accommodated by a major west-dipping structure. Our results are in general consistent with the studies of Giambiagi et al. (2015) and Farías et al. (2010) but our refined hypocenter locations better highlight the general alignment of the seismicity along a large-scale structure extending beneath the Frontal Cordillera and the Principal Cordillera. At the Frontal-Principal Cordillera transition (∼70°W), in particular beneath the Aconcagua fold-and-thrust belt, this structure is well-defined, lying at ∼10 km depth, with a low dipping angle (5–7° to the west). The Aconcagua fold-and-thrust belt is identified in many east-vergent models (e.g., Giambiagi et al., 2015) as a former deep-rooted (5–10 km depth) Andean deformation front, active between ∼20 and ∼10 Ma, and totalling a cumulative crustal shortening of ∼45 km. The connection between the Aconcagua fold-and-thrust belt and this structure is thus tempting. However, a recent reevaluation of the geometry and cumulative shortening suggests that the Aconcagua fold-and-thrust belt is in fact very shallow with a décollement level no deeper than 2–3 km and the associated cumulative shortening no larger than 10 km (Riesner et al., 2018). These observations confirm that the Aconcagua Fold-and-Thrust belt corresponds to a secondary feature that was carried up during the uplift of the Frontal Cordillera basement, controlled by a deeper structure (Armijo et al., 2010; Figure 2b). Interestingly, Two of our focal mechanism solutions (2 and 4 in Table 1 and Figure 8a) exhibit fault planes compatible with the idea that the west-dipping structure inferred from our seismicity catalog (Figure 8) accommodates compressive stress and could be responsible for the uplift of the Frontal Cordillera. However, we acknowledge that despite their relatively high magnitude (Ml = 3.4 and 3.7) compared to the rest of the catalog ($1.5 > Ml > 2.0$), these events could be associated with secondary faults rather than larger regional structures.

Recent constraints on the timing of deformation (Riesner et al., 2019) evidenced that the exhumation of the Frontal Cordillera started ∼20 Ma, which implies that this décollement must have been active during that time. Although the Cuyo basin lacks seismological instrumentation and therefore no seismicity is observed east of 70°W, the Andean basal decollement identified in this work could potentially connect to the faults identified in the eastern part of the Frontal Cordillera and farther east, to recent Pliocene uplifts (Figure 1). Since there are no deformation markers in the Cuyo basin prior to 7–10 Ma (Giambiagi et al., 2003), this connection must be posterior to 7–9 Ma and could suggest an eastward migration of the deformation front. We acknowledge that these interpretations relate to tectonic features located at the edge of our study region and are consequently, not fully backed up by our tomographic images or our seismicity catalog. The deployment of seismometers in the eastern part of the Frontal Cordillera and in the Cuyo basin would be particularly useful to extend our observations and refine the seismotectonic interpretations of this area.

It is interesting to note that our focal mechanisms located in the Principal Cordillera (events 1, 6, and 7 in Table 1 and Figure 8), beneath the volcanic arc, are characterized by a strong strike-slip component. Previous studies evidenced a strong relationship between transpressive tectonics and the southern Chile volcanic arc, between 35oS and 48oS along the liquine-Ofqui fault (Cembrano & Lara, 2009; De Pascale et al., 2021). The transpressive

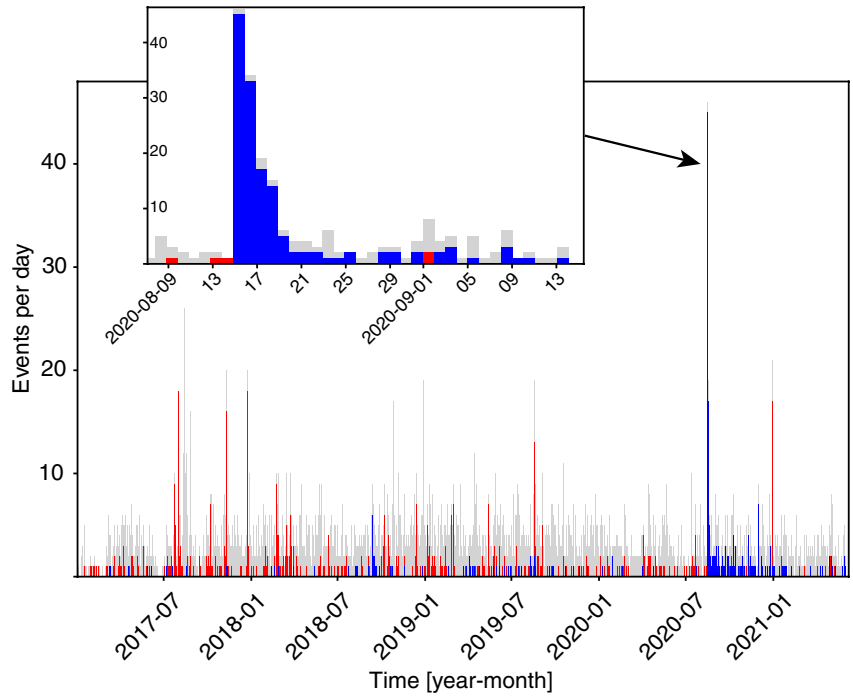

Figure 9. Daily variations of the seismicity rate for all the crustal events described in this work (gray) as well as two clusters of interest: C1 and C4 (See main text and Figure 8). The inset shows with more details the seismic sequence following the 15 August 2020 11:11 earthquake (Table 1) corresponding to cluster C4.

character of intermediate magnitude events in the Principal Cordillera was also inferred after the occurrence of the Las Melosas earthquake, the largest crustal event instrumentally recorded in the South-Central Andes. This earthquake occurred on 4 September 1958 in the Principal Cordillera, ~60 km southeast from Santiago (Figures 1 and 8a). Alvarado et al. (2009) were able to estimate a moment magnitude of Mw 6.3 associated with a strike-slip focal mechanism, in agreement with observations made on local seismograms (Pardo & Acevedo, 1984). Another crustal event (Alvarado et al., 2005) which occurred in 2001, close to event 1 (Table 1, Figure 8a) also characterized by a strike-slip focal mechanism, strengthening the idea that transpressive stress is being accommodated along the volcanic arc, in the Principal Cordillera (Figure 8). However, unlike the liquine-Ofqui fault in the Southern Andes volcanic arc, no apparent large-scale strike-slip structure has been identified in the South-Central Andes.

Our focal mechanism solutions with a more pronounced reverse component (events 2, 3, 4, and 5 in Table 1 and Figure 8) are consistent with NE-SW crustal shortening accommodation along the west-dipping structure inferred from our improved seismicity catalog although we acknowledge that the limited number of focal mechanisms does not allow robust seismotectonic interpretations. However, regional stress tensor as well as the GNSS velocity field of the Chilean margin (Ammirati et al., 2019; Métois et al., 2016) indicate that crustal shortening in the South-Central Andes is controlled by the Nazca plate subduction. The observation of both strike-slip and reverse mechanisms in this area suggests that the accommodation of the NE-SW Nazca-South America convergence could be partitioned between the west-dipping décollement inferred from our seismicity catalog and secondary strike-slip crustal fractures affecting the Principal Cordillera crust, beneath the volcanic arc. In our study area, some authors pointed out the role of such fractures in terms of increasing crustal permeability and the rise of magma toward the surface (Piquer Romo et al., 2019).

A seismicity cluster (C4 in Figure 8) is located in the Principal Cordillera at 33.2°S; 70°W. It contains the highest magnitude crustal event ($Mw = 4.8$, event 2 in Table 1) characterized during our period of observation (15 August 2020 11:11 UTC). The distribution of the seismicity within this cluster mostly follows the occurrence of the 15 August 2020 earthquake, forming a sequence of 227 events (Figure 9). We note that the seismicity rate after the main event exponentially decreases from ~45 events/day to 1 event/day in ~10 days, resembling a classical aftershock sequence (Omori, 1984). Although the location of this sequence is aligned with the volcanic arc, it is

located about 20 km north from the Tupungato–Tupungatito complex (Figures 1, 7 and 8) that marks the northern termination of the Southern Andean volcanic zone (Cembrano and Lara. 2009). Two of the focal mechanism solutions obtained in this work correspond to events from this sequence, including the 15 August 2020 event (events 6 and 7 in Table 1 and Figure 8). Fault plane solutions (Table 1) are compatible with strike-slip motion and thus suggest that this sequence would be related to the accommodation of the transpressive stress induced by the oblique Nazca-South America convergence.

5.2.2. Frontal Cordillera

To the west, beneath the FC (~70.4°W), the seismic activity appears deeper (~15–20 km depth) and more diffuse. The alignment of this seismicity suggests the presence of a steeper structure (17–19° to the west) compared to the observations made further east (Figure 8). The geology of this area (Figure 1) is characterized by the volcano-sedimentary Abanico and Farellones formations (Thiele, 1980). These formations, deposited between 31 and 16 Ma (Charrier et al., 2005), are deformed by a series of high-angle, east-dipping faults rooting on a ~12–15 km depth décollement (Riesner et al., 2018). Following the idea that the main Andean basal décollement would be a west-dipping structure with an east-propagating deformation front, the West Andean fold-and-thrust belt and the West Andean Thrust would correspond to antithetic (backthrust) faults. Some authors pointed out the role of inherited extensional, high-angle structures, in the creation of mountain belts under compressive regimes (e.g., Amilibia et al., 2008). In the case of the West Andean Fold-and-Thrust belt, these faults could be inherited from the Miocene extension of the Abanico basin and later reactivated during the Andean compression thus currently accommodating the shortening and uplift of the Principal Cordillera (Charrier et al., 2005; Mardones et al., 2021). The Coastal Cordillera basement, well identified in our tomographic images of the Chilean forearc (Figures 5, 6b, 7) is a rigid block (Farías et al., 2010) that could play an important role in the uplift of the Principal Cordillera, by acting as a backstop transferring the Nazca-South American plates convergence forces toward the east.

The abrupt topographic step between the Principal Cordillera and the Central depression characterizes the West Andean Thrust, the most recent surface manifestation of crustal shortening and uplift of the Principal Cordillera. At ~33.5°S, the structure responsible for this uplift is a well-identified reverse fault known as the San Ramón fault, the scarp of which has been clearly identified at the piedmont of the Principal Cordillera and bordering the eastern limits of the city of Santiago (Armijo et al., 2010; Vargas et al., 2014). Previous seismotectonic studies (Ammirati et al., 2019) showed that the San Ramón fault plane, defined between its scarp at the surface and the seismogenic zone at 12–15 km depth, was large enough to generate a Mw = 7.5 earthquake, matching observations of large events that ruptured the San Ramón fault in the past ~20 kyr (Vargas et al., 2014), but almost no seismic events were located directly close to the surface on the San Ramón fault plane. The improved seismicity catalog presented here does include some hypocenters distributed along an east-dipping structure compatible with the inferred geometry of the San Ramón fault at depth (Figures 8c and 8d). It is important to note that the San Ramón fault represents a limited segment of the study area and other faults along the West Andean Thrust, such as the Infernillo fault and Quaternary faults along the Pocuro fault system area (Figures 1 and 8a), show a similar configuration to what can be observed at ~33.5°S (i.e., the thrusting of the Principal Cordillera over the Quaternary deposits of the Central depression). Hence, we do not discard potential connections of these structures at depth.

The seismicity cluster C1 (Figures 6a and 6b) located 25–30 km beneath the metropolitan area of Santiago (Central Depression) corresponds to the well-identified Santa Rosa cluster (Leyton et al., 2009; Ammirati et al., 2019). It contains 444 of our relocated events (Figures 7a and 8d). Previous studies (e.g., Farias et al., 2010) tried to link this cluster to the extension at depth of the WAT but the connection is not obvious, in particular because the cluster is very localized and therefore presents no alignment with the exposed regional structures (Figures 7a and 8).

We observe on Figures 5 and 6b that C1 tops a zone of relatively high crustal velocities (Vp > 6.8 km/s) and Vp/Vs ratio (~1.8) suggesting a mafic composition of the crust at those depths. Such a composition would explain the possibility of brittle failure deeper than 15–20 km (Hacker, 1996). As discussed before, this area beneath the Central Depression marks the transition between the Coastal Cordillera basement to the west and the Cordilleran basement to the east. Although this thinner and denser crust seems to exhibit a N-S extension (from 34 to 32.5°S; Figures 5, 6b,7a, and 7b), the reason for the nucleation of earthquakes in this specific area remains unclear. The seismicity rate is quite constant over our period of observation (Figure 9) with about 1–2 events per day and punctually jumps to 15–17 events/day. It is interesting to note that these bumps of seismic activity do not last more than a couple of days. More importantly, they are not preceded by a larger event nor characterized

by an exponential decrease of activity as generally observed for aftershock sequences (Omori, 1984). In view of these elements, the Santa Rosa cluster could be related to fluid circulations as evidenced by Contreras-Reyes et al. (2021) for the forearc of northern Chile.

6. Conclusions

In this study, we processed 4.4 years (January 2017 to May 2021) of continuous waveform data recorded by the Chilean permanent seismic network, using a deep-learning approach. The resulting P and S travel time picks are combined and inverted with a dataset from a previous temporary seismic deployment, resulting in tomographic models of seismic velocities in the Chilean foreland crust with an unprecedented level of detail. The improved velocity models are used to compute 3-D probabilistic hypocenter locations resulting in a robust catalog of more than ∼14,000 events. Finally, double-difference relocations revealed structural details related to crustal shortening of the South-Central Andes. The tomographic models and improved hypocenter distribution are combined in order to reevaluate the conceptual model of crustal deformation along a key cross section at latitude 33.5°S. The distribution of the crustal seismicity suggests the presence of an active west-dipping major structure that likely accommodated the uplift of the Frontal Cordillera for the past 20 Myr. The west Andean front is seismically active and could accommodate the uplift of the Principal Cordillera along structures compatible with backthrust faults. The basement of the Coastal Cordillera is likely acting as a backstop and would transfer stress from the subduction toward the east.

Transpressive focal mechanisms solutions observed for a few earthquakes in the Principal Cordillera suggest that secondary shallow structures located beneath the volcanic arc could accommodate the oblique (NE-SW) Nazca-South American convergence.

Data Availability Statement

Raw seismic waveforms used in this study are available from the IRIS platform (https://ds.iris.edu/ds/nodes/dmc/). Network codes are C1, C, and G. Data preparation and preprocessing were performed using the ObsPy package (Beyreuther et al., 2010). Most of the figures were made with the Generic Mapping Tools (GMT) package (Wessel & Smith, 2006) and the Matplotlib library (Hunter, 2007).

Acknowledgments
This research has been supported by the Agencia Nacional de Investigación y Desarrollo (ANID) of Chile (FONDECYT grant N3200633). AV acknowledges the institutional support of the "Severo Ochoa Centre of Excellence" accreditation (CEX2019-000928-S). We thank Tony Monfret for providing the phase information and station metadata from the CHASE temporary experiment. We are grateful to the editor, Isabelle Manighetti as well as two anonymous reviewers for their very constructive comments and suggestions.

References

Alvarado, P., Barrientos, S., Saez, M., Astroza, M., & Beck, S. (2009). Source study and tectonic implications of the historic 1958 Las Melosas crustal earthquake, Chile, compared to earthquake damage. *Physics of the Earth and Planetary Interiors*, *175*(1/2), 26–36. https://doi.org/10.1016/j.pepi.2008.03.015

Alvarado, P., Beck, S., Zandt, G., Araujo, M., & Triep, E. (2005). Crustal deformation in the south-central Andes back-arc terranes as viewed from regional broadband seismic waveform modeling. *Geophysical Journal International*, *163*(2), 580–598. https://doi.org/10.1111/j.1365-246X.2005.02759.x

Amilibia, A., Sàbat, F., McClay, K. R., Muñoz, J. A., Roca, E., & Chong, G. (2008). The role of inherited tectono-sedimentary architecture in the development of the central Andean mountain belt: Insights from the Cordillera de Domeyko. *Journal of Structural Geology*, *30*, 1520–1539. https://doi.org/10.1016/j.jsg.2008.08.005

Ammirati, J.-B., Vargas, G., Rebolledo, S., Abrahami, R., Potin, B., Leyton, F., & Ruiz, S. (2019). The crustal seismicity of the Western Andean thrust (Central Chile, 33°-34°S): Implications for regional tectonics and seismic hazard in the Santiago area. *Bulletin of the Seismological Society of America*, *109*(5), 1985–1999. https://doi.org/10.1785/0120190082

Araya Vargas, J., Meqbel, N. M., Ritter, O., Brasse, H., Weckmann, U., Yáñez, G., & Godoy, B. (2019). Fluid distribution in the Central Andes subduction zone imaged with magnetotellurics. *Journal of Geophysical Research: Solid Earth*, *124*(4), 4017–4034. https://doi.org/10.1029/2018JB016933

Armijo, R., Rauld, R., Thiele, R., Vargas, G., Campos, J., Lacassin, R., & Kausel, E. (2010). The West Andean thrust, the San Ramon fault, and the seismic hazard for Santiago, Chile. *Tectonics*, *29*(2), TC2007. https://doi.org/10.1029/2008TC002427

Barrientos, S., & National Seismological Center (CSN) Team. (2018). The seismic network of Chile. *Seismological Research Letters*, *89*(2A), 467–474. https://doi.org/10.1785/0220160195

Barrientos, S., Vera, E., Alvarado, P., & Monfret, T. (2004). Crustal seismicity in central Chile. *Journal of South American Earth Science*, *16*, 759–768. https://doi.org/10.1016/j.jsames.2003.12.001

Benz, H. M., Chouet, B. A., Dawson, P. B., Lahr, J. C., Page, R. A., & Hole, J. A. (1996). Three dimensional P and S wave velocity structure of Redoubt volcano, Alaska. *Journal of Geophysical Research*, *101*(B4), 8111–8128. https://doi.org/10.1029/95JB03046

Beyreuther, M., Barsch, R., Krischer, L., Megies, T., Behr, Y., & Wassermann, J. (2010). ObsPy: A Python toolbox for seismology. *Seismological Research Letters*, *81*(3), 530–533. https://doi.org/10.1785/gssrl.81.3.530

Brocher, T. M. (2005). Empirical relations between elastic wavespeeds and density in the Earth's crust. *Bulletin of the Seismological Society of America*, *95*(6), 2081–2092. https://doi.org/10.1785/0120050077

Capitanio, F. A., Faccenna, C., Zlotnik, S., & Stegman, D. R. (2011). Subduction dynamics and the origin of Andean orogeny and the Bolivian orocline. *Nature*, *480*(7375), 83–86. https://doi.org/10.1038/nature10596

Carlson, R. L., & Miller, D. J. (1997). A new assessment of the abundance of serpentinite in the oceanic crust. *Geophysical Research Letters*, *24*(4), 457–460. https://doi.org/10.1029/97GL00144

Carlson, R. L., & Miller, D. J. (2003). Mantle wedge water contents estimated from seismic velocities in partially serpentinized peridotites. *Geophysical Research Letters*, *30*(5), 1250. https://doi.org/10.1029/2002GL016600

Cembrano, J., & Lara, L. (2009). The link between volcanism and tectonics in the southern volcanic zone of the Chilean Andes: A review. *Tectonophysics*, *471*(1–2), 96–113. https://doi.org/10.1016/j.tecto.2009.02.038

Charrier, R., Bustamante, M., Comte, D., Elgueta, S., Flynn, J. J., Iturra, N., et al. (2005). The Abanico extensional basin: Regional extension, chronology of tectonic inversion and relation to shallow seismic activity and Andean uplift. *Neues Jahrbuch für Geologie und Paläontologie - Abhandlungen*, *236*, 43–77. https://doi.org/10.1127/njgpa/236/2005/43

Christensen, N. I., & Mooney, W. D. (1995). Seismic velocity structure and composition of the continental crust: A global view. *Journal of Geophysical Research*, *100*(B7). https://doi.org/10.1029/95JB00259

Condit, C. B., Guevara, V. E., Delph, J. R., & French, M. E., (2020). Slab dehydration in warm subduction zones at depths of episodic slip and tremor. *Earth and Planetary Science Letters*, *552*, 116601. https://doi.org/10.1016/j.epsl.2020.116601

Contreras-Reyes, E., Díaz, D., Bello-González, J. P., Slezak, K., Potin, B., Comte, D., et al. (2021). Subduction zone fluids and arc magmas conducted by lithospheric deformed regions beneath the central Andes. *Scientific Reports*, *11*(1), 1–12. https://doi.org/10.1038/s41598-021-02430-9

De Pascale, G. P., Froude, M., Penna, I., Hermanns, R. L., Sepúlveda, S. A., Moncada, D., et al. (2021). Liquiñe-Ofqui's fast slipping intra-volcanic arc crustal faulting above the subducted Chile Ridge. *Scientific Reports*, *11*, 7069. https://doi.org/10.1038/s41598-021-86413-w

Delouis, B., Nocquet, J. M., & Vallée, M. (2010). Slip distribution of the February 27, 2010 Mw = 8.8 Maule earthquake, central Chile, from static and high-rate GPS, InSAR, and broadband teleseismic data. *Geophysical Research Letters*, *37*(17), L17305. https://doi.org/10.1029/2010GL043899

DeMets, C., Gordon, R. G., & Argus, D. F. (2010). Geologically current plate motions. *Geophysical Journal International*, *181*, 1–80. https://doi.org/10.1111/j.1365-246X.2009.04491.x

Ekström, G., Nettles, M., & Dziewoński, A. M. (2012). The global CMT project 2004-2010: 649 centroid-moment tensors for 13,017 earthquakes. *Physics of the Earth and Planetary Interiors*, *200–201*, 6501–6509. https://doi.org/10.1016/j.pepi.2012.04.002

Farías, M., Compte, D., Charrier, R., Martinod, J., David, C., Tassara, A., et al. (2010). Crustal-scale structural architecture in central Chile based on seismicity and surface geology: Implications for Andean mountain building. *Tectonics*, *29*, TC3006. https://doi.org/10.1029/2009TC002480

Fromm, R., Zandt, G., & Beck, S. (2004). Crustal thickness beneath the Andes and Sierras Pampeanas at 30∘S inferred from Pn apparent phase velocities. *Geophysical Research Letters*, *31*, 1–4. https://doi.org/10.1029/2003GL019231

Giambiagi, L., Ramos, V., Godoy, E., Alvarez, P. P., & Orts, S. (2003). Cenozoic deformation and tectonic style of the Andes between 33° and 34° south latitude. *Tectonics*, *22*(4), 1041. https://doi.org/10.1029/2001TC001354

Giambiagi, L., Tassara, A., Mescua, J., Tunik, M., Alvarez, P. P., Godoy, E., et al. (2015). *Evolution of shallow and deep structures along the Maipo-Tunuyan transect (33 40'S): From the Pacific Coast to the Andean Foreland* Geological Society of London, Special Publication, 399, 63–82. https://doi.org/10.1144/SP399.14

Gilbert, H., Beck, S., & Zandt, G. (2006). Lithospheric and upper mantle structure of central Chile and Argentina. *Geophysical Journal International*, *165*, 383–398. https://doi.org/10.1111/j.1365-246X.2006.02867.x

GVP. (2022). Global volcanism Program, Smithsonian institution, National Museum of natural history – List of Holocene volcanoes. Retrieved from https://volcano.si.edu/list_volcano_holocene.cfm

Hacker, B. R. (1996). Eclogite formation and the rheology, buoyancy, seismicity, and H_2O content of oceanic crust. *Geophysical Monograph Series* (Vol. 96, pp. 337–346). American Geophysical Union.

Hayes, G. (2018). *Slab2 - A comprehensive subduction zone geometry model*. U.S. Geological Survey data release. https://doi.org/10.5066/F7PV6JNV

Hildreth, W., & Moorbath, S. (1988). Crustal contributions to arc magmatism in the Andes of central Chile. *Contributions to Mineralogy and Petrology*, *98*(4), 455–489.

Hilley, G. E., Strecker, M. R., & Ramos, V. A. (2004). Growth and erosion of fold-and-thrust belts with an application to the Aconcagua fold-and-thrust belt, Argentina. *Journal of Geophysical Research*, *109*. https://doi.org/10.1029/2002JB002282

Hunter, J. D. (2007). Matplotlib: A 2D Graphics environment. *Computer Science and Engineering*, *9*(3), 90–95. https://doi.org/10.1109/MCSE.2007.55

Kay, S. M., Godoy, E., & Kurtz, A. (2005). Episodic arc migration, crustal thickening, subduction erosion, and magmatism in the south-central Andes. *The Geological Society of America Bulletin*, *117*(1–2), 67–88. https://doi.org/10.1130/B25431.1

Lay, T., Yue, H., Brodsky, E. E., & An, C. (2014). The 1 April 2014 Iquique, Chile, Mw 8.1earthquake rupture sequence. *Geophysical Research Letters*, *41*(11), 3818–3825. https://doi.org/10.1002/2014GL060238

Leyton, P., Pérez, A., & Campos, J. (2009). Anomalous seismicity in the lower crust of the Santiago basin, Chile. *Physics of the Earth and Planetary Interior*, *175*, 17–25. https://doi.org/10.1016/j.pepi.2008.03.016

Lomax, A., Virieux, J., Volant, P., & Berge, C. (2000). Probabilistic earthquake location in 3D and layered models: Introduction of a Metropolis-Gibbs method and comparison with linear locations. In C. H.Thurber, & N.Rabinowitz (Eds.), *Advances in seismic event location* (p. 101). Amsterdam: Kluwer

Mardones, V., Peña, M., Pairoa, S., Ammirati, J. B., & Leisen, M. (2021). Architecture, kinematics, and tectonic evolution of the principal cordillera of the Andes in Central Chile (∼ 33.5°S): Insights From Detrital Zircon U-Pb Geochronology and Seismotectonics Implications. *Tectonics*, *40*(7), e2020TC006499.

Marot, M., Monfret, T., Gerbault, M., Nolet, G., Ranalli, G., & Pardo, M. (2014). Flat versus normal subduction zones: A comparison based on 3-D regional traveltime tomography and petrological modelling of central Chile and Western Argentina (29º–35ºS). *Geophysical Journal International*, *199*, 1633–1564. https://doi.org/10.1093/gji/ggu355

Marot, M., Monfret, T., Pardo, M., Ranalli, G., & Nolet, G. (2013). A double seismic zone in the subducting juan Fernández ridge of the Nazca plate (32∘S), central Chile. *Journal of Geophysical Research*, *118*(7), 3462–3475. https://doi.org/10.1002/jgrb.50240

Mcquarrie, N. (2002). Initial plate geometry, shortening variations, and evolution of the Bolivian orocline. *Geology*, *30*(10), 867–870. https://doi.org/10.1130/0091-7613(2002)030<0867:IPGSVA>2.0

Mernagh, T. P., Leys, C., & Henley, R. W. (2020). Fluid inclusion systematics in porphyry copper deposits: The super-giant Grasberg deposit, Indonesia, as a case study. *Ore Geology Reviews*, *123*, 103570. https://doi.org/10.1016/j.oregeorev.2020.103570

Métois, M., Vigny, C., & Socquet, A. (2016). Interseismic coupling, megathrust earthquakes and seismic swarms along the Chilean subduction zone (38°-18°S). *Pure and Applied Geophysics*, *173*, 1431–1449. https://doi.org/10.1007/s00024-016-1280-5

Mingorance, F. (2006). Morfometría de la escarpa de falla histórica identificada al norte del cerro La Cal, zona de falla La Cal, Mendoza. *Revista de la Asociación Geológica Argentina*, *61*, 620–638.
Nash, J. T., & Theodore, T. G. (1971). Ore fluids in the porphyry copper deposit at Copper Canyon, Nevada. *Economic Geology*, *66*(3), 385–399. https://doi.org/10.2113/gsecongeo.66.3.385
Omori, F. (1894). On the aftershocks of earthquake. *Journal of College of Science, Imperial University of Tokyo*, *7*, 111–200.
Paige, C. C., & Saunders, M. A. (1982). LSQR: An algorithm for sparse linear equations and sparse least squares. *ACM Transactions on Mathematical Softwares*, *8*, 43–71. https://doi.org/10.1145/355984.355989
Pardo, M., & Acevedo, P. (1984). Mecanismos de foco en la zona de Chile Central. *Tralka*, *2*(3), 279–293.
Pichowiak, S. (1994). Early Jurassic to early Cretaceous magmatism in the coastal cordillera and the central depression of north Chile. In *Tectonics of the southern Central Andes* (pp. 203–217). Berlin, Heidelberg: Springer.
Piquer Romo, J., Yáñez, G., Rivera, O., & Cooke, D. (2019). Long-lived crustal damage zones associated with fault intersections in the high Andes of Central Chile. *Andean Geology*, *46*(2), 223–239. https://doi.org/10.5027/andgeoV46n2-3106
Podvin, P., & Lecomte, I. (1991). Finite difference computation of traveltimes in very contrasted velocity models: A massively parallel approach and its associated tools. *Geophysical Journal International*, *105*(1), 271–284.
Porter, R., Gilbert, H., Zandt, G., Beck, S., Warren, L., Calkins, J., et al. (2012). Shear wave velocities in the Pampean flat-slab region from Rayleigh wave tomography: Implications for slab and upper mantle hydration. *Journal of Geophysical Research*, *117*(B11). https://doi.org/10.1029/2012JB009350
Ramos, V. A. (2000). Evolución tectónica de la Argentina. In R.Caminos (Ed.), Geología Argentina Servicio Geológico Minero Argentino (Vol. 29, pp. 715–784). Buenos Aires: Instituto de Geología y Recursos Minerales.
Ramos, V. A., & Folguera, A. (2009). Andean flat-slab subduction through time. *Geological Society, London, Special Publications*, *327*, 31–54.
Riesner, M., Lacassin, R., Simoes, M., Armijo, R., Rauld, R., & Vargas, G. (2017). Kinematics of the active west Andean fold-and-thrust belt (Central Chile): Structure and long-term shortening rate. *Tectonics*, *36*, 287–303. https://doi.org/10.1002/2016TC004269
Riesner, M., Lacassin, R., Simoes, M., Carrizo, D., & Armijo, R. (2018). Revisiting the crustal structure and kinematics of the Central Andes at 33.5°S: Implications for the mechanics of Andean mountain building. *Tectonics*, *37*, 1347–1375. https://doi.org/10.1002/2017TC004513
Riesner, M., Simoes, M., Carrizo, D., & Lacassin, R. (2019). Early exhumation of the frontal cordillera (southern central Andes) and implications for andean mountain-building at ∼33.5ºS. *Scientific Reports*, *9*, 7972. https://doi.org/10.1038/s41598-019-44320-1
Ruiz, S., Aden-Antoniow, F., Baez, J. C., Otarola, C., Potin, B., delCampo, F., et al. (2017). Nucleation phase and dynamic inversion of the Mw 6.9 Valparaíso earthquake in Central Chile. *Geophysical Research Letters*, *44*(20), 10290–10297. https://doi.org/10.1002/2017GL075675
Ruiz, S., Klein, E., delCampo, F., Rivera, E., Poli, P., Metois, M., et al. (2016). The seismic sequence of the 16 September 2015, Illapel Mw 8.3 earthquake. *Seismological Research Letters*. https://doi.org/10.1785/0220150281
Ruiz, S., & Madariaga, R. (2018). Historical and recent large megathrust earthquakes in Chile. *Tectonophysics*, *733*, 37–56. https://doi.org/10.1016/j.tecto.2018.01.015
Sdrolias, M., & Müller, R. D. (2006). Controls on back-arc basin formation. *Geochemistry Geophysics Geosystems*, *7*(4). https://doi.org/10.1029/2005GC001090
Sokos, E. N., & Zahradnik, J. (2008). ISOLA a Fortran code and a Matlab GUI to perform multiple-point source inversion of seismic data. *Computers and Geoscience*, *34*(8), 967–977. https://doi.org/10.1016/j.cageo.2007.07.005
Spencer, C., & Gubbins, D. (1980). Travel-time inversion for simultaneous earthquake location and velocity structure determination in laterally varying media. *Geophysical Journal International*, *63*(1), 95–116. https://doi.org/10.1111/j.1365-246X.1980.tb02612.x
Tarantola, A., & Valette, B. (1982). Generalized nonlinear inverse problems solved using the least squares criterion. *Reviews of Geophysics*, *20*(2), 219–232. https://doi.org/10.1029/RG020i002p00219
Thiele, R. (1980). *Geología de la hoja Santiago, Región Metropolitana, Carta Geológica de Chile*. Scale 1:250,000. (pp. 51). Instituto de Investigaciones Geológicas.
Tryggvason, A., Rögnvaldsson, S. T., & Flóvenz, Ó. G. (2002). Three-dimensional imaging of the P- and S-wave velocity structure and earthquake locations beneath Southwest Iceland. *Geophysical Journal International*, *151*, 848–866. https://doi.org/10.1046/j.1365-246X.2002.01812.x
Vackář, J., Burjánek, J., Gallovič, F., Zahradník, J., & Clinton, J. (2017). Bayesian ISOLA: New tool for automated centroid moment tensor inversion. *Geophysical Journal International*, *210*(2), 693–705. https://doi.org/10.1093/gji/ggx158
Vargas, G., Klinger, Y., Rockwell, T. K., Forman, S. L., Rebolledo, S., Baize, S., et al. (2014). Probing large intraplate earthquakes at the west flank of the Andes. *Geology*, *42*(12). https://doi.org/10.1130/G35741.1
Vergara, M., López-Escobar, L., Palma, J. L., Hickey-Vargas, R., & Roeschmann, C. (2004). Late tertiary volcanic episodes in the area of the city of Santiago de Chile: New geochronological and geochemical data. *Journal of South American Earth Science*, *17*, 227–238. https://doi.org/10.1016/j.jsames.2004.06.003
Wagner, L. S., Beck, S., & Zandt, G. (2005). Upper mantle structure in the south central Chilean subduction zone (30º to 36ºS). *Journal of Geophysical Research*, *110*(B1). https://doi.org/10.1029/2004JB003238
Waldhauser, F., & Ellsworth, W. L. (2000). A double-difference earthquake location algorithm: Method and application to the Hayward Fault, California. *Bulletin of the Seismological Society of America*, *90*(6), 1353–1368. https://doi.org/10.1785/0120000006
Watanabe, T. (1993). Effects of water and melt on seismic velocities and their application to characterization of seismic reflectors. *Geophysical Research Letters*, *20*(24), 2933–2936. https://doi.org/10.1029/93GL03170
Wessel, P., & Smith, W. H. F. (2006). New, improved version of generic mapping tools released. *EOS Transactions American Geophysical Union*, *79*(47), 579. https://doi.org/10.1029/98EO00426
Zhang, M., Ellsworth, W., & Beroza, G. (2019). Rapid earthquake association and location. *Seismological Research Letters*, *90*(6), 2276–2284. https://doi.org/10.1785/0220190052
Zhu, W., & Beroza, G. (2019). PhaseNet: A deep-neural-network-based arrival time picking method. *Geophysical Journal International*, *216*, 261–273. https://doi.org/10.1093/gji/ggy423